

# Low Carrier Effective Masses in Photoactive $\text{Sr}_2\text{Sb}_2\text{O}_2\text{Q}_3$ ( $\text{Q} = \text{S}, \text{Se}$ ): The Role of the Lone Pair

Sandy Al Bacha, Sébastien Saitzek, Pascal Roussel, Marielle Huvé, Emma E. McCabe,\* and Houria Kabbour\*



Cite This: *Chem. Mater.* 2023, 35, 9528–9541



Read Online

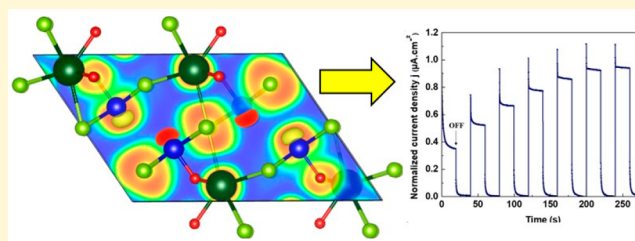
ACCESS |

Metrics & More

Article Recommendations

Supporting Information

**ABSTRACT:** The crystal structure, electronic properties, photocatalytic activity, and photocurrent response of a new antimony oxysulfide  $\text{Sr}_2\text{Sb}_2\text{O}_2\text{S}_3$  and its oxyselenide analogue  $\text{Sr}_2\text{Sb}_2\text{O}_2\text{Se}_3$  are presented. Both oxychalcogenides contain heteroleptic  $\text{SbOQ}_4$  units with stereochemically active  $5s^2$  electron pairs. Our combined experimental and computational study highlights the structure–property relationships in this family of materials. By means of density functional theory calculations, we show very low effective masses for the electrons ( $m_e^* = 0.191(6)$  and  $0.163(2) m_0$ ) and holes ( $m_h^* = 0.276(2)$  and  $0.190(2) m_0$ ) for the oxysulfide and the oxyselenide, respectively, an indication of very high mobilities. Using DFT calculations, we attribute the low effective mass values (related to the curvature of the bands) to the nature and strength of the bonding between the lone pair electrons and the anions in the studied structure compared with other structure ( $\text{Sr}_6\text{Cd}_2\text{Sb}_6\text{S}_{10}\text{O}_7$ ). We analyze the states contributing to the lone pair stereoactivity and consequently to the observed photocurrent response and photocatalytic behavior under solar irradiation. This activity, the band gap values, and the band edge positions illustrate the potential of these antimony oxychalcogenides as promising candidates for water splitting using solar energy. Our study unlocks some key features in designing oxychalcogenides with low effective masses, which are advantageous for photocatalysis.



## INTRODUCTION

The sustainable production of hydrogen, for energy production using fuel cells, is a current goal in our challenge to meet society's energy demands.<sup>1</sup> Photocatalytic water splitting is one route to produce hydrogen and is sustainable if it can be achieved using visible light (rather than higher energy UV radiation). However, the use of visible light places constraints on the photocatalytic semiconductor: it must have a band gap in the range of 1.23–3.1 eV, and its conduction band minimum (CBM) and valence band maximum (VBM) must be compatible with the redox potential of water (i.e., the CBM more negative than the reduction potential of  $\text{H}_2\text{O}/\text{H}_2$  (0 V) and the VBM more positive than the oxidation potential of  $\text{O}_2/\text{H}_2\text{O}$  (1.23 V)).<sup>2</sup> While many oxide photocatalysts have shown good performance (such as  $\text{K}_2\text{La}_2\text{Ti}_3\text{O}_{10}$  (2186 and 1131  $\mu\text{mol}\cdot\text{h}^{-1}$  for  $\text{H}_2$  and  $\text{O}_2$  evolution, respectively)<sup>3</sup> and  $\text{Bi}_2\text{MO}_6$  ( $k_{\text{app}} = 6.3 \times 10^{-3}$  and  $1.7 \times 10^{-3} \text{ min}^{-1}$  for W and Mo, respectively, for rhodamine B degradation<sup>4</sup>), they typically have large band gaps (e.g., 3.5 eV for  $\text{K}_2\text{La}_2\text{Ti}_3\text{O}_{10}$ ) and are only photocatalytically active under UV irradiation.<sup>5–8</sup> This has motivated researchers to turn toward mixed-anion materials in the search for stable and efficient visible light photocatalysts.<sup>9,10</sup> On the other hand, the Aurivillius phases  $\text{Bi}_2\text{MO}_6$  ( $M = \text{Mo}, \text{W}$ ) have smaller band gaps (2.6 and 2.8 eV for  $\text{Bi}_2\text{MoO}_6$  and  $\text{Bi}_2\text{WO}_6$ , respectively) due in part to the contribution from  $\text{Bi}^{3+} 6s^2$  states to the top of the valence

band,<sup>4</sup> suggesting that “inert pair”  $ns^2$  cations (such as  $\text{Sb}^{3+}$ ) might be advantageous in tuning the band gap in potential photocatalysts.

Oxychalcogenides have attracted attention due to their wide range of properties, including magnetism,<sup>11,12</sup> photocatalysis, and electrochemistry.<sup>13,14</sup> In the context of visible-light water splitting, oxysulfides were seen as potential photocatalysts because the sulfide's lower electronegativity (compared with oxide anions) can lead to an increase in the valence band potential and therefore a decrease in the band gap to the visible range.<sup>15</sup> Within the oxychalcogenide family, many materials adopt layered structures that allow the ordering of the anions into more ionic ( $\text{O}^{2-}$ ) and more covalent ( $\text{Q}^{2-} = \text{S}^{2-}, \text{Se}^{2-}, \text{Te}^{2-}$ ) layers.<sup>16</sup> The layered crystal structure tends to give a highly anisotropic electronic band structure, interesting electronic properties, and high mobilities of charge carriers.<sup>17</sup> Finally, depending on the judicious choice of ions, oxychalcogenides with heteroleptic ( $\text{O}^{2-}$  and  $\text{Q}^{2-}$ ) coordination of key cations can also be prepared. These heteroleptic

Received: May 26, 2023

Revised: September 27, 2023

Published: October 23, 2023



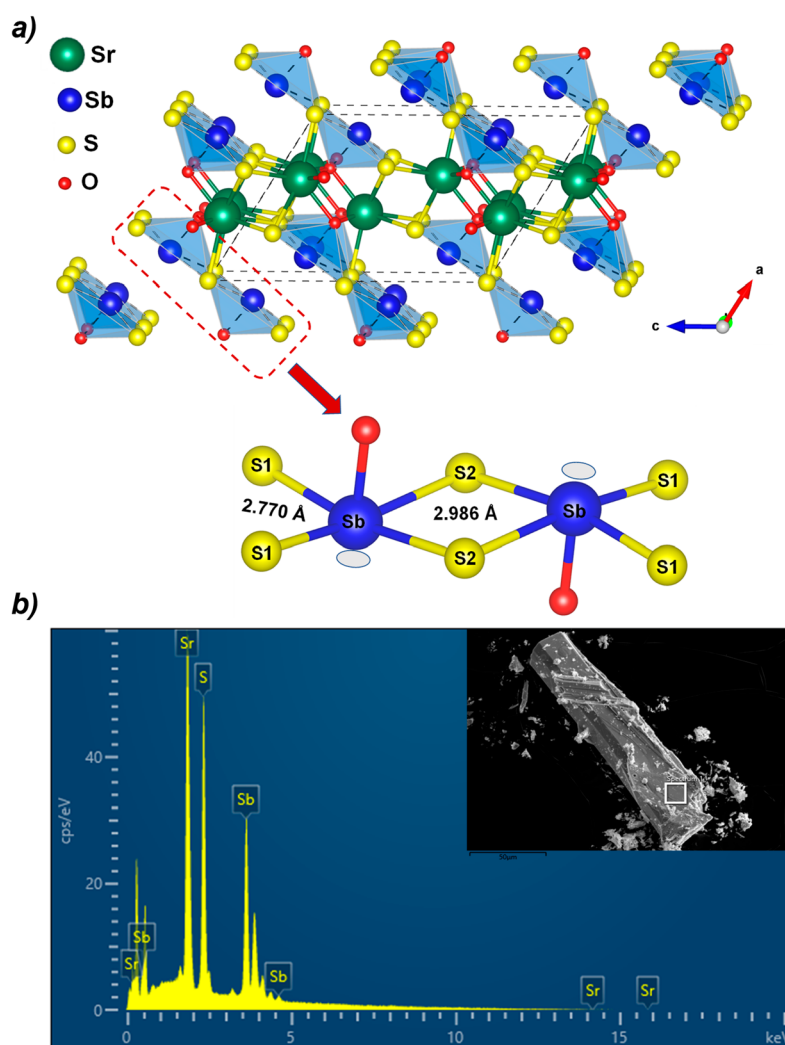


**Figure 1.** (a) View of the  $P2_1/c$  model of  $\text{Sr}_2\text{Sb}_2\text{O}_2\text{S}_3$  with the coordination environments and distances of Sb ions. (b) Spectrum of the EDX analysis of a  $\text{Sr}_2\text{Sb}_2\text{O}_2\text{S}_3$  crystal.

coordination environments are often polar, which can enhance electron–hole separation to give better photocatalytic performance.<sup>18–20</sup> According to the literature, several oxysulfides were found to be stable with good performances for water splitting with a suitable band gap energy in the visible range.  $\text{Y}_2\text{Ti}_2\text{O}_5\text{S}_2$  demonstrated its stability with efficient stoichiometric production for both  $\text{H}_2$  and  $\text{O}_2$ ,<sup>21</sup> and  $\text{LaOInS}_2$  polymorphs exhibited interesting  $\text{H}_2$  production.<sup>22,23</sup>

Another important feature for photocatalysis is the dynamics of the charge carriers, their effective masses, and thus their mobility, which can have an impact on the semiconductor performance.<sup>24,25</sup> Oxide materials with differences in the effective masses of their charge carriers exhibit a difference in character between the valence and conduction band,<sup>26</sup> as the VB tends to be flat because of the localized oxygen p character, giving large hole effective masses, while the CB is more dispersive because of the contribution of cations, giving low electron effective masses.<sup>27,28</sup> For example, in a typical post-transition metal-based oxide semiconductor with low electrons and holes effective masses, both CBM and VBM are dispersed because of the unoccupied 5s orbitals of the post-transition metal and the orbitals of the neighboring cations overlapping, as well as the interaction of the occupied post transition metal

5s/3d orbitals with anion p orbitals, respectively.<sup>29–32</sup> On the other hand, a recent study on tin oxyselenide demonstrated that introducing a chalcogenide  $\text{Q}^{2-}$  with its higher energy level and larger ionic radius can reduce the bulk/interface trap states, leading to an enhanced carrier mobility.<sup>33</sup> A small number of oxysulfides and oxyselenides have gained attention for their low holes effective masses such as tetragonal-ZrOS ( $0.24 m_0$ ) and cubic-ZrOS ( $0.37 m_0$ ),<sup>34</sup>  $\text{SnSe}_x\text{O}_{1-x}$  ( $m_h^* = 0.58, 0.93, 1.99$  for  $x = 0.22, 0.56,$  and  $0.74$ , respectively).<sup>33</sup>

We report here  $\text{Sr}_2\text{Sb}_2\text{O}_2\text{S}_3$  oxysulfide, an analog to the recently discovered oxyselenide  $\text{Sr}_2\text{Sb}_2\text{O}_2\text{Se}_3$  that adopts a structure comprising double chains of edge-linked  $\text{SbSe}_4\text{O}$  square-based pyramids (Figure 1a).<sup>35</sup> Alongside the synthesis and structural characterization of these antimony oxychalcogenides, diffuse reflectance measurements suggest direct band gaps of 2.44(1) and 1.72(1) eV for  $\text{Sr}_2\text{Sb}_2\text{O}_2\text{S}_3$  and  $\text{Sr}_2\text{Sb}_2\text{O}_2\text{Se}_3$ , respectively, well matched to the solar spectrum. Photocurrent measurements revealed that both materials exhibit an activity under sunlight with and without external potential, as well as the capacity to degrade rhodamine B. Electronic structure calculations indicate that the top of the valence band is primarily composed of  $\text{Sb}^{3+}$  and  $\text{S}^{2-}/\text{Se}^{2-}$

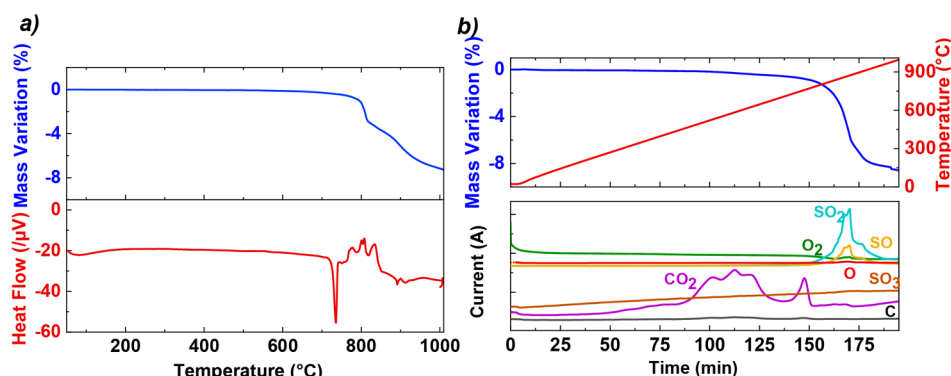


**Figure 2.** (a) TGA spectrum (upper panes) and TDA spectrum (lower panes) of  $\text{Sr}_2\text{Sb}_2\text{O}_2\text{S}_3$  under argon. (b) TGA spectra (upper pane) and mass spectra (lower pane) of  $\text{Sr}_2\text{Sb}_2\text{O}_2\text{S}_3$  under argon. The mass variation and temperature are given as a function of time.

states, as well as revealed very low electron and hole effective masses, indicating high mobilities for both compositions.

## METHODS

Single-phase samples of  $\text{Sr}_2\text{Sb}_2\text{O}_2\text{Q}_3$  ( $\text{Q} = \text{S}, \text{Se}$ ) (1 g) were synthesized by a solid-state reaction from stoichiometric mixtures of the precursors:  $\text{SrS}/\text{Sb}_2\text{O}_3/\text{Sb}/\text{S}$  (Alfa Aesar 99.5%) in the molar ratio 2:0.667:0.667:1 for the oxysulfide and  $\text{SrO}/\text{Sb}/\text{Se}$  (Alfa Aesar 99.5%) in the molar ratio 2:2:3 for the oxyselenide. Mixing and grinding were carried out in an argon-filled glovebox due to the air sensitivity of some reactants. Mixtures were then pelletized and heated in an evacuated and sealed carbon-coated quartz tube. Thermal treatment consisted of heating up to 700 and 800 °C for  $\text{Sr}_2\text{Sb}_2\text{O}_2\text{S}_3$  and  $\text{Sr}_2\text{Sb}_2\text{O}_2\text{Se}_3$ , respectively, at a rate of 70 °C·h<sup>-1</sup> and dwelling for 48 h before cooling to room temperature. Upon grinding the pellets, orange and gray powders were obtained for the oxysulfide and the oxyselenide, respectively.

Powder X-ray diffraction (XRPD) data were collected on a Bruker D8 A25 diffractometer equipped with a Lynxeye XET linear detector ( $\text{Cu K}\alpha$ ) in the Bragg–Brentano geometry at room temperature with a 1 s counting time and 0.02° step angle. Rietveld refinements were carried out using Topas Academic software.<sup>36,37</sup> The background, sample height, lattice parameters, peak profiles, atomic positions, and global atomic displacement parameter (per phase) were refined. XRPD data were collected in reflection mode, and a preferred orientation was observed in some sets of data as a result of the sample packing method. This was modeled in Rietveld refinements using a March–Dollase function along one direction.<sup>38</sup> Despite this additional correction in the refinements, they demonstrate the high quality of the samples prepared.

A transmission electron microscopy diffraction study was performed on an FEI Technai G2–20 twin microscope. The powder was crushed and dropped in the form of an alcohol suspension on carbon-supported copper grids, followed by evaporation under ambient conditions.

Diffuse-reflectance of the sample was measured from 200 to 900 nm using a PerkinElmer Lambda 650 spectrophotometer.

Scanning electron microscopy (SEM) experiments and energy dispersive X-ray (EDX) analysis were carried out on a Hitachi S3400N microscope.

The thermal stability of  $\text{Sr}_2\text{Sb}_2\text{O}_2\text{S}_3$  was investigated by thermogravimetric analysis (TGA) using a TGA-92 thermobalance under pure argon; TGA was coupled with thermal dilatometric analysis (TDA) at first, then with mass spectrometry (MS). The evolved gases were monitored by an Omnistar quadrupole mass spectrometer (Pfeiffer). The atmosphere was controlled by evacuating and then filling the thermobalance with the carrier gas before the sample was heated to 1000 °C at a rate of 5 °C·min<sup>-1</sup>.

Density functional theory (DFT) calculations were carried out using the projector-augmented-wave method<sup>39,40</sup> encoded in the

Vienna *ab initio* simulation package (VASP)<sup>41</sup> and the generalized gradient approximation (GGA) of Perdew, Burke, and Ernzerhof (PBE)<sup>42</sup> for the exchange–correlation functionals. Full geometry optimizations were carried out using a plane-wave energy cutoff of 550 eV and the k-points mesh (4 × 13 × 3). The precise electronic structure calculations were then carried out with a threshold of the self-consistent-field energy convergence of 10<sup>-6</sup> eV and with the k-points mesh (6 × 20 × 5) in the irreducible Brillouin zone for  $\text{Sr}_2\text{Sb}_2\text{O}_2\text{Q}_3$  ( $\text{Q} = \text{S}, \text{Se}$ ). The relaxed structure was a good match (reasonable deviation not exceeding few percentages for the unit cell parameters) with the experimental structure (see unit cell parameters and atomic positions of the relaxed structures in the SI), and it was used for calculations of the electronic band structure, the effective masses of the charge carriers, and the density of states. Vesta software<sup>43</sup> was used to visualize the crystal structure and the localized electron densities. The crystal orbital Hamiltonian population (COHP) analysis was carried out in the framework of the LOBSTER software.<sup>44–46</sup>

The photoreactor consisted of a 200 mL flask irradiated from above and aluminum foil covers to prevent radiation exposure. First, the solution (containing 200 mL of rhodamine B (5 × 10<sup>-6</sup> mol dm<sup>-3</sup>) and 100 mg of the photocatalyst powder ( $\text{Sr}_2\text{Sb}_2\text{O}_2\text{Q}_3$  ( $\text{Q} = \text{S}, \text{Se}$ ))) were placed in an ultrasound for 20 min (to break up agglomerates), and the mixture was stirred for 30 min in the dark to ensure an appropriate adsorption–desorption equilibrium. This test was performed under UV (254 nm, 40 W) and solar (100 mW cm<sup>-2</sup>) irradiations. Then, samples were taken at regular intervals to monitor the evolution of the concentration of the photodegraded rhodamine B by spectrophotometry. Absorbance measurements were carried out using a Shimadzu UV-2600 UV–visible spectrophotometer.

The electrochemical device (Autolab PGSTAT204, Metrohm) coupled to an LED module (LED driver kit, Metrohm) was used to collect the photocurrent measurements. The LEDs (450, 470, 505, 530, 590, and 627 nm with low spectral dispersion) were calibrated using a photodiode to determine the density of the luminous flux received by the sample. The photoelectrochemical measurements were performed in standard three-electrode cell (Magnetic Mount Photoelectrochemical Cell (Redox.me)), including Ag/AgCl and Pt wire acting as the reference electrode and counter electrode, respectively. This cell allows standardized illumination over 1 cm<sup>2</sup> by the backside of the working electrode. The working electrode consisted of the photocatalyst powder dispersed in PVDF (polyvinylidene fluoride) binder (in 2:1 ratio), which was later deposited on an ITO/glass substrate (Delta Technologies, Ltd.) using the drop casting technique.<sup>47</sup> The electrolyte employed is an aqueous 0.1 M sodium sulfate ( $\text{Na}_2\text{SO}_4$ ) solution.

## RESULTS

**Polycrystalline Phase Analysis.** Small single crystals of  $\text{Sr}_2\text{Sb}_2\text{O}_2\text{S}_3$  were first identified by serendipity in some

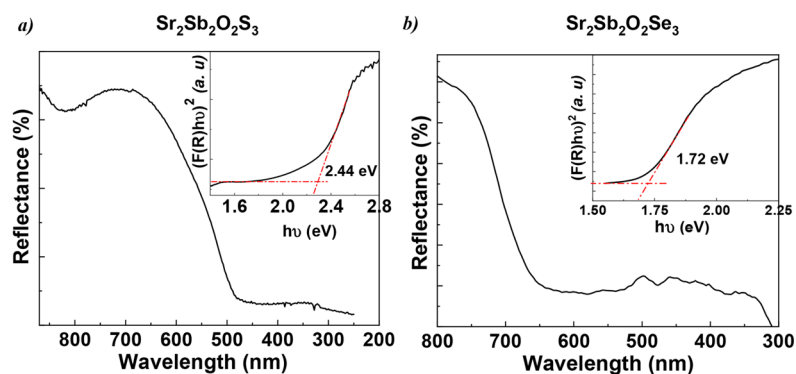


Figure 3. Diffuse-reflectance spectra with a Tauc plot inset to determine the experimental band gaps of (a)  $\text{Sr}_2\text{Sb}_2\text{O}_2\text{S}_3$  and (b)  $\text{Sr}_2\text{Sb}_2\text{O}_2\text{Se}_3$ .

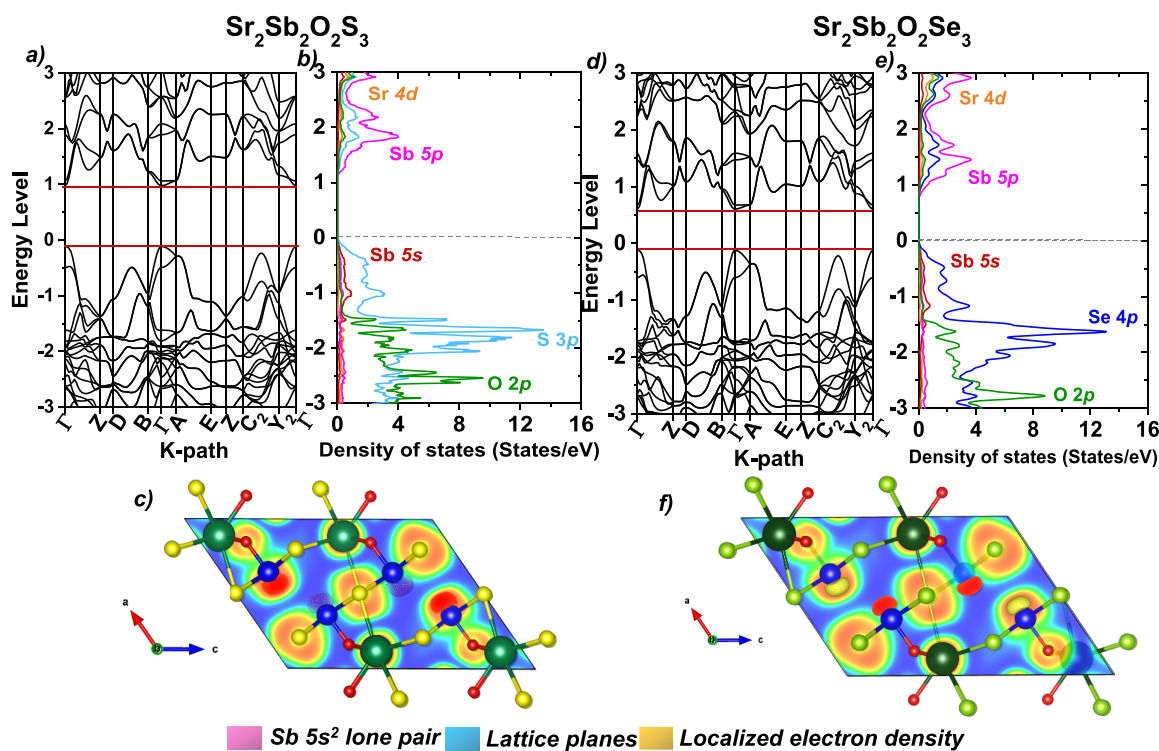


Figure 4. (a and d) Electronic band structures of  $\text{Sr}_2\text{Sb}_2\text{O}_2\text{S}_3$  and  $\text{Sr}_2\text{Sb}_2\text{O}_2\text{Se}_3$ , respectively. (b and e) Projected DOS shown for the Sr 4d, Sb 5s, Sb 5p, S 3p/Se 4p, and O 2p states of  $\text{Sr}_2\text{Sb}_2\text{O}_2\text{S}_3$  and  $\text{Sr}_2\text{Sb}_2\text{O}_2\text{Se}_3$ , respectively. The Fermi level is set to 0. (c and f) Local electron density projected on the (010) lattice plane and 0.91 isosurface levels of DFT plots of  $\text{Sr}_2\text{Sb}_2\text{O}_2\text{S}_3$  and  $\text{Sr}_2\text{Sb}_2\text{O}_2\text{Se}_3$ , respectively, for the  $P2_1/c$  model.

attempts to prepare another compound, namely  $\text{Sr}_6\text{Zn}_2\text{Sb}_6\text{O}_7\text{S}_{10}$ . After optimizing the synthesis method for  $\text{Sr}_2\text{Sb}_2\text{O}_2\text{S}_3$ , a high-purity sample (without Zn) was prepared. The method was optimized using stoichiometric amounts of reagents based on preliminary investigations using single crystal X-ray diffraction and EDX and then finding the optimal synthesis temperature of 700 °C, as noted above. Preliminary analysis of XRPD data (see the Supporting Information) indicated a model consistent with the previously reported Se analogue,  $\text{Sr}_2\text{Sb}_2\text{O}_2\text{Se}_3$ ,<sup>35</sup> in the  $P2_1/c$  space group with, as expected, a slightly smaller unit cell volume (room temperature volume of 404.68 (2) Å<sup>3</sup> (see SI) compared with 432.81 Å<sup>3</sup> for  $\text{Sr}_2\text{Sb}_2\text{O}_2\text{Se}_3$ ). EDX analysis of the Sr, Sb, and S content revealed a Sr:Sb:S ratio of 28.3:29.0:42.7, in good agreement with the expected stoichiometry of  $\text{Sr}_2\text{Sb}_2\text{O}_2\text{S}_3$  (Figure 1b). A sample of  $\text{Sr}_2\text{Sb}_2\text{O}_2\text{Se}_3$  was also prepared following the method reported by Panella et al.<sup>35</sup>

Other distortions to give various C-centered monoclinic structural models were also considered but gave no significant improvement in fit. Alternately, a preliminary crystallographic study using single crystal X-ray diffraction and electron diffraction data was conducted, which revealed a more complex structure: electron diffraction data reveal additional reflections that can only be indexed by incommensurately modulated structures, which may vary between domains (see the Supporting Information). A more detailed structural study is underway.

**Thermal Stability.** The thermal stability of  $\text{Sr}_2\text{Sb}_2\text{O}_2\text{S}_3$  was studied using TGA coupled with TDA (Figure 2a) and then coupled with mass spectrometry under argon, in both cases going up to 1000 °C (Figure 2b). No weight loss was associated with the endothermic peak at ~735 °C on the TDA curve (lower panes), suggesting a phase transition at this temperature. Above 800 °C, two weight losses were detected



coupled with three exothermic combined peaks that indicated phase degradation. A structural phase transition could not be confirmed by high temperature XRD due to insufficient information about the fusion temperature.

To investigate possible phase degradation, TGA was coupled with MS with the same conditions (under argon in the range 25–1000 °C). No loss of water was observed (no signal at  $m/z$  18). Signals were measured (lower panes) at  $m/z$  64 ( $\text{SO}_2^+$ ),  $m/z$  48 ( $\text{SO}^+$ ), and  $m/z$  44 ( $\text{CO}_2$ ), allowing the evolved gases to be identified. A sharp mass loss (8.1%) occurs at around 800 °C, close to the theoretical mass loss expected for the loss of one molecule of sulfur monoxide (SO) (8.8%). This was confirmed by EDX (see the Supporting Information) on the residue after TGA-MS measurements, where the atomic percentages corresponding to the sulfur element decreased.

**Optical Measurements.** Optical properties of the polycrystalline  $\text{Sr}_2\text{Sb}_2\text{O}_2\text{S}_3$  and  $\text{Sr}_2\text{Sb}_2\text{O}_2\text{Se}_3$  phases were investigated by measuring the diffuse reflectance using UV–visible spectroscopy. The reflectance vs wavelength analysis is shown in Figure 3. The Kubelka–Munk transformation  $F(R) = (1 - R)^{(1/n)}/2R^{48}$  was applied to the reflectance, and the optical band gap,  $E_g$ , was determined using the Tauc plot method<sup>49</sup> by drawing  $[F(R)hv]^{1/n}$  vs  $[hv]$  (where  $hv$  is the photon energy). Assuming a direct allowed transition ( $n = 1/2$ ) (see the results from DFT calculations, presented below),  $E_g$  was determined to be 2.44(1) and 1.72(1) eV for  $\text{Sr}_2\text{Sb}_2\text{O}_2\text{S}_3$  and  $\text{Sr}_2\text{Sb}_2\text{O}_2\text{Se}_3$ , respectively; these values are convenient for the solar spectrum, and comparable with other reported mixed-anion materials including oxynitrides  $\text{LaTiO}_2\text{N}$  (2.1 eV),<sup>50</sup>  $\text{XNbO}_2\text{N}$  ( $X = \text{Ca}, \text{Sr}, \text{Ba}, \text{La}$ ),<sup>51</sup> and lone-pair-containing oxyfluorides  $\text{Bi}_2\text{NbO}_5\text{F}$  (2.86 eV),  $\text{Bi}_2\text{TaO}_5\text{F}$  (2.95 eV).<sup>52</sup>

**First-Principles Calculations.** DFT calculations were carried out to investigate the electronic band structures of  $\text{Sr}_2\text{Sb}_2\text{O}_2\text{Q}_3$ ; calculations were carried out using both the reported  $P2_1/c$  models and the higher symmetry  $C2/m$  models (described above). This choice of symmetry has a minimal effect on the results from these electronic structure calculations (because the additional parameters allowed by the  $P2_1/c$  model are in fact very close to the ideal values of the  $C2/m$  model). Results for the  $P2_1/c$  models are presented here, while those for the  $C2/m$  models are given in the Supporting Information for comparison. DFT calculations revealed direct band gaps of 1.09 and 0.73 eV for  $Q = \text{S}, \text{Se}$ , respectively. These are smaller than the experimental optical band gaps (2.44(1) and 1.72 eV measured for  $\text{Sr}_2\text{Sb}_2\text{O}_2\text{S}_3$  and  $\text{Sr}_2\text{Sb}_2\text{O}_2\text{Se}_3$ , respectively) discussed above. This might be explained by the GGA approximation (with the PBE functional used here), which is well-known to underestimate band gaps.<sup>42</sup> Figure 4a and d show the calculated electronic band structure for  $\text{Sr}_2\text{Sb}_2\text{O}_2\text{Q}_3$  with valence band maximum and conduction band minimum at the  $\Gamma$  point (0; 0; 0) for both  $Q = \text{S}, \text{Se}$ .

The projected densities of states are shown in Figure 4b and e, focusing on the region around the Fermi level of the valence and conduction band. The orbitals near this selected region are mainly dominated by Sb and S/Se states, while Sr and the O states make a minimal contribution. The Sb 5p states dominate the conduction band minimum, lying from  $\sim 1$  to  $\sim 3$  eV, while the Sb 5s states lie in the valence band (in the range of  $-1.5$  to  $-0.1$  eV), hybridizing with the O 2p and S 3p/Se 4p to form the maximum of the valence band. This orbital contribution to both bands was also confirmed by the plot of the fat bands (see

the Supporting Information), and similar results have been reported for  $\text{Sm}_2\text{Ti}_2\text{S}_2\text{O}_5$ ,<sup>53</sup> and  $\text{Ln}_2\text{Ti}_2\text{S}_2\text{O}_5$ .<sup>54</sup>

A similar Sb 5s contribution to the top of the valence band was also observed for several antimony-based compounds, including  $\text{Sr}_6\text{Cd}_2\text{Sb}_6\text{S}_{10}\text{O}_7$  oxysulfide;<sup>55,20</sup>  $\alpha$ - $\text{Sb}_2\text{O}_3$ ,  $\beta$ - $\text{Sb}_2\text{O}_3$ ,  $\gamma$ - $\text{Sb}_2\text{O}_3$ ,  $\alpha$ - $\text{Sb}_2\text{O}_4$  and  $\beta$ - $\text{Sb}_2\text{O}_4$  oxides;<sup>56</sup> and  $\text{Sb}_2\text{S}_3$  and  $\text{Sb}_2\text{Se}_3$  chalcogenide semiconductors.<sup>57</sup> This Sb 5s–Q  $np$  ( $Q = \text{O}, \text{S}, \text{Se}$ ) hybridization plays a key role in reducing the band gap into the visible range.

In order to have a quantitative investigation of the charge carriers' mobilities, the effective masses of electrons ( $m_e^*$ ) and of holes ( $m_h^*$ ) were calculated<sup>58</sup> using the following equation near the CBM and the VBM at  $\Gamma$  (0; 0; 0):

$$\left(\frac{1}{m^*}\right)_{ij} = \frac{1}{\hbar^2} \frac{\partial^2 E_n(k)}{\partial k_i \partial k_j} \quad (1)$$

where  $E_n(k)$  corresponds to the  $n$ -th electronic band in  $k$ -space. Prior to the effective masses' extraction, the self-consistent electronic calculation was followed by a non-self-consistent calculation along the high symmetry lines. Different dispersions were observed at the CBM and VBM, suggesting different mobilities for the electrons and holes. We investigated the directions within the layers,  $\Gamma \rightarrow \text{A}$ ,  $\Gamma \rightarrow \text{B}$ ,  $\Gamma \rightarrow \text{Z}$ , and  $\Gamma \rightarrow \text{Y}_2$ , very near to the  $\Gamma$  point, since the VBM and the CBM are located at  $\Gamma$  for both phases.

The calculations revealed low effective masses for both oxyselenide and oxysulfide phases (Table 1), with particularly

**Table 1. Calculated Electron ( $m_e^*$ ) and Hole ( $m_h^*$ ) Effective Masses<sup>a</sup> for  $\text{Sr}_2\text{Sb}_2\text{O}_2\text{Q}_3$  for the  $P2_1/c$  model**

| direction                       | $\text{Sr}_2\text{Sb}_2\text{O}_2\text{S}_3$ |             | $\text{Sr}_2\text{Sb}_2\text{O}_2\text{Se}_3$ |             |
|---------------------------------|--|-------------|---|-------------|
|                                 | $m_e^*/m_0$                                  | $m_h^*/m_0$ | $m_e^*/m_0$                                   | $m_h^*/m_0$ |
| $\Gamma \rightarrow \text{A}$   | 1.958(8)                                     | 0.718(4)    | 1.393(1)                                      | 0.447(7)    |
| $\Gamma \rightarrow \text{B}$   | 0.651(8)                                     | 0.276(2)    | 0.428(3)                                      | 0.190(2)    |
| $\Gamma \rightarrow \text{Z}$   | 0.191(6)                                     | 0.848(7)    | 0.163(2)                                      | 0.525(2)    |
| $\Gamma \rightarrow \text{Y}_2$ | 1.681(2)                                     | 1.482(2)    | 1.656(2)                                      | 1.013(1)    |

<sup>a</sup> $m_0$  being the free electron rest mass.

low values for the electron (0.163(2)  $m_0$  for  $\Gamma \rightarrow \text{Z}$ ) and hole (0.190(2)  $m_0$  for  $\Gamma \rightarrow \text{B}$ ) effective masses for the oxyselenide. The carrier mobility is inversely proportional to the effective mass; therefore, this high mobility makes the oxyselenide particularly attractive for efficient photoconduction and photocatalysis applications. These values are lower than those reported for related oxyselenide and oxysulfide materials ( $m_e^*$  values of 0.59 and 0.68  $m_0$  for  $\text{BiCuOS}$  and  $\text{BiAgOS}$ , respectively;<sup>59</sup>  $m_h^*$  of 0.24 and 0.37  $m_0$  for  $c$ -ZrOS and  $t$ -ZrOS, respectively;<sup>34</sup>  $m_e^* = 1.6(2)$   $m_0$  for  $\text{LaCuOSe}$ ;<sup>60</sup>  $m_h^* = 0.58$ , 0.93, and 1.99  $m_0$  for  $\text{SnSe}_x\text{O}_{1-x}$ ).<sup>33</sup> The high mobilities reflect the high dispersion at the VBM and CBM, which is influenced by both the high covalency (particularly for the oxyselenide), and the presence of the stereochemically active 5s<sup>2</sup> electron pair on  $\text{Sb}^{3+}$  ions (as discussed further below).

The Sb 5s–Q  $np$  hybridization relates to the Sb 5s<sup>2</sup> lone pair and its stereochemical activity. The valence electron density map projected on the (010) plane is shown in Figure 4c and f, giving insight into the stereoactivity of the  $\text{Sb}^{3+}$  lone pair within the  $\text{O}(\text{S}, \text{Se})_4$  heteroleptic environment. More generally, the stereochemical activity of lone pairs is known to bring crystalline anisotropy, and the positive effects of lone pairs on several properties have been put forward in different types of

materials. Recently, theoretical studies have been reported for reduced main group cations (in oxides), such as the lone pair cation  $\text{Sn}^{2+}$  (discussed later, ref 84), where the high mobility of the charge carriers is mostly related to the lone pair states and the overlap between the  $s$  orbital of the lone pair cation and the anions states. Another example in chalcogenides are the well-known  $\text{Sb}_2\text{S}_3$  and  $\text{Sb}_2\text{Se}_3$  semiconductors, which were also theoretically studied for lone pair-related anisotropic effects (effective masses and mobility) to provide guidelines for using their features to design efficient solar cells devices.<sup>57</sup> Similar effects were also observed for Sb-based compounds,<sup>61</sup> such as  $\text{Sr}_6\text{Cd}_2\text{Sb}_6\text{S}_7\text{O}_{10}$ <sup>20</sup> and  $\text{Sr}_6\text{Cd}_2\text{Sb}_6\text{Se}_7\text{O}_{10}$ ,<sup>19</sup> and a Bi-based compound with a  $6s^2$  stereoactive lone pair.<sup>62</sup>

To quantify this stereochemical activity, a universal method described by Hu et al.<sup>63,64</sup> was adopted to calculate the ratio of the stereochemical activity  $R_{\text{SCA}}$ , which involves integrating the PDOS of Sb states from a specified energy level (the point where the intensity of Sb  $s$  and Sb  $p$  is equivalent) to the Fermi level (set at 0). This makes the  $R_{\text{SCA}}$  sensitive to the choice of energy range depending on the orbitals of the chosen lone pair cation.  $R_{\text{SCA}}$  was calculated to be 0.68 and 0.54 for the antimony lone pair within the  $\text{SbS}_4\text{O}$  and  $\text{SbSe}_4\text{O}$  entities, respectively (Table 2 and Supporting Information). In our

**Table 2. Integrated PDOS from a Specified Energy Level to the Fermi Level and the Calculated Stereochemical Activity Factor for the  $\text{SbS}_4\text{O}$  and  $\text{SbSe}_4\text{O}$  Entities**

|                   | $\text{SbS}_4\text{O}$ entity | $\text{SbSe}_4\text{O}$ entity |
|-------------------|-------------------------------|--------------------------------|
| $I(\text{Sb } s)$ | 1.6                           | 1.3                            |
| $I(\text{Sb } p)$ | 2.33                          | 2.39                           |
| $R_{\text{SCA}}$  | 0.68                          | 0.54                           |

previous study on  $\text{Sr}_6\text{Cd}_2\text{Sb}_6\text{S}_{10}\text{O}_7$ ,<sup>20</sup> we found  $R_{\text{SCA}}$  values of 0.57, 0.59, and 0.64 for  $\text{SbS}_5$ ,  $\text{SbS}_4\text{O}$ , and  $\text{SbO}_3$ , respectively. This is an indication that the presence of an heteroleptic environment (coordinated with both sulfide/selenide and oxide anions) around the antimony influences its stereochemical activity; as the anion ionicity increases, this activity also increases (see ref 20 and references therein in which the correlation with the DFT calculated lone pair volume is also consistent with this evolution).

The crystal orbital hamiltonian population (COHP) calculation gives access to not only projected contributions on specific bonds with the dispersion but also an integral value representing the nature (bonding/antibonding) and average strength of the bond. The ICOHP obtained for some representative border distances seems to have an evolution mostly depending on the distance, with similar average distances in both compounds. On the other hand, the dispersion of the p-COHP allows a better comparative study (Figure 5). In the case of the  $\text{Sr}_2\text{Sb}_2\text{S}_3\text{O}_2$  phase, the Sb–S antibonding states (that relate to the Sb  $5s^2$  lone pair, as defined by the revised model<sup>65,66</sup>) extend from the Fermi level much deeper into the valence band compared with  $\text{Sr}_6\text{Cd}_2\text{Sb}_6\text{S}_{10}\text{O}_7$ .<sup>20</sup> It is equivalent to greater curvature of bands used to determine the  $m_{\text{h}}^*$  and constitute one explanation for the lower  $m_{\text{h}}^*$  in  $\text{Sr}_2\text{Sb}_2\text{S}_3\text{O}_2$ .

**Electrochemical Measurements.** The chronoamperometric measurements (showing the variation in current density  $\Delta j$  as the difference between the illuminated ( $j_{\text{ill}}$ ) and the dark current densities ( $j_{\text{dark}}$ )) were carried out for  $\text{Sr}_2\text{Sb}_2\text{O}_2\text{Q}_3$  ( $Q = \text{S}, \text{Se}$ ). Measurements were carried out for thick films of

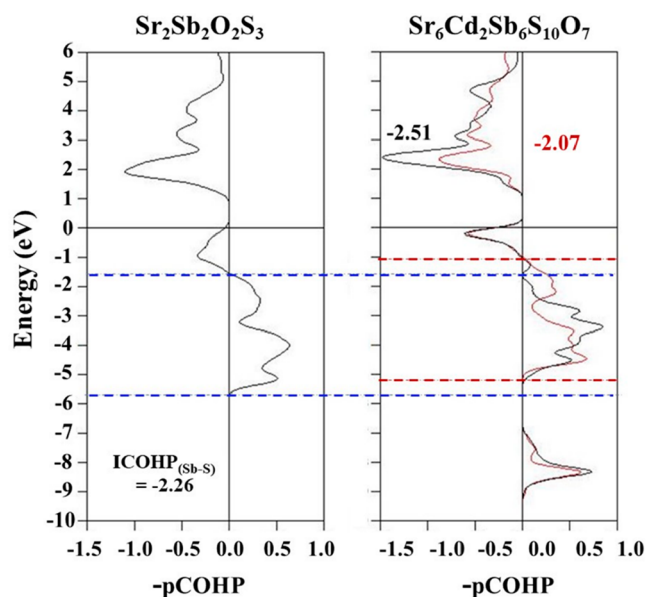


**Figure 5.** (left) Projected COHP (p-COHP) for the  $\text{Sr}_2\text{Sb}_2\text{O}_2\text{S}_3$  phase on one of the 1D unit “border” Sb–S bonds calculated with the  $C2/m$  optimized structure and (right) p-COHP for the phase  $\text{Sr}_6\text{Cd}_2\text{Sb}_6\text{S}_{10}\text{O}_7$  on the Sb–S bonds located at two opposite borders of the 1D (in red and black) unit. Dashed blue and red lines represent the extent of the Sb–S antibonding states in the valence band and of the lower bonding states.

$\text{Sr}_2\text{Sb}_2\text{O}_2\text{S}_3$  under 450 nm light with several irradiances for illumination and dark cycles (Figure 6). Without an external bias voltage, the transient photocurrent increased from  $1.7 \times 10^{-1} \mu\text{A}\cdot\text{cm}^{-2}$  for a  $22 \text{ mW}\cdot\text{cm}^{-2}$  power density to  $2.2 \times 10^{-1} \mu\text{A}\cdot\text{cm}^{-2}$  for  $42 \text{ mW}\cdot\text{cm}^{-2}$  and kept increasing more slowly until reaching a stable photocurrent of  $2.65 \times 10^{-1} \mu\text{A}\cdot\text{cm}^{-2}$  for  $111 \text{ mW}\cdot\text{cm}^{-2}$  (Figure 6a). Figure 6b presents the evolution of the photocurrent  $\Delta j$  with the intensity of the luminous flux  $\Phi_0$  according to a classical power law,<sup>67</sup> giving a curve going through the origin with an equation of  $\Delta j = (8.10 \times 10^{-2})\Phi_0^{0.25}$ . For an ideal trap-free system, the exponent is equal to 1. In our case, the fitting gives a nonunity (i.e., 0.25(2)) exponent, suggesting a complex process of electron–hole generation, recombination, and trapping within the sample. Moreover, for high light intensities, the photocurrent becomes independent of the light intensity received. This effect can be due to a saturation of photogenerated electron–hole pairs and/or a limitation of mobility in the layer.<sup>68</sup> The same measurements were performed under 0.4 V bias voltage, where the value of the current density increases with the voltage (see the Supporting Information). However, the trend remains the same with a power law whose exponent is low (0.18(2)) indicating that for high powers most of the traps are already filled in and further illumination power cannot effectively increase the photogain.<sup>69</sup>

The produced photocurrent is naturally linked to the material’s absorption; therefore, for an orange powder, the best efficiency should be observed in the complementary color spectral area between 450 and 505 nm. This was confirmed by recording the variation of the transient photocurrent  $\Delta j$  for  $V_{\text{bias}} = 0 \text{ V}$  vs wavelength (Figure 6c). The highest photocurrent was observed at 505 nm, and it decreased toward the longest wavelengths (590–627 nm). This result was also observed

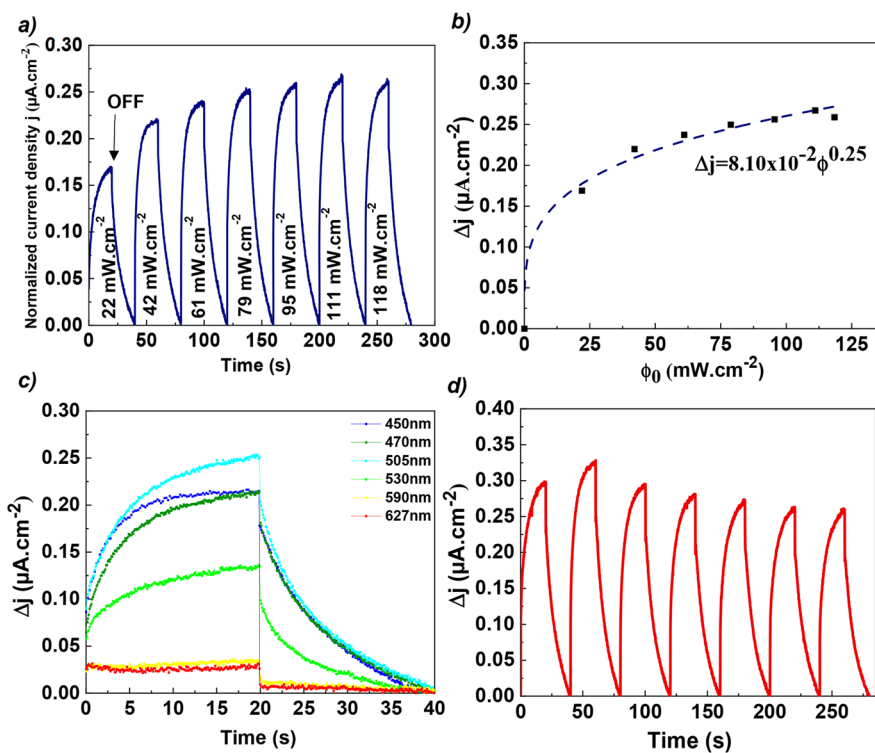


**Figure 6.** (a) Transient photocurrent response ( $V_{\text{bias}} = 0$  V under a 450 nm excitation) of  $\text{Sr}_2\text{Sb}_2\text{O}_2\text{S}_3$ . (b) Evolution of the photocurrent density the power density of light. (c) Transient photocurrent response vs wavelengths (constant light intensity  $\phi_0 = 42$   $\text{mW cm}^{-2}$  and  $V_{\text{bias}} = 0$  V) of  $\text{Sr}_2\text{Sb}_2\text{O}_2\text{S}_3$ . (d) Transient photocurrent response under solar illumination ( $100$   $\text{mW cm}^{-2}$ ) for  $V_{\text{bias}} = 0$  V.

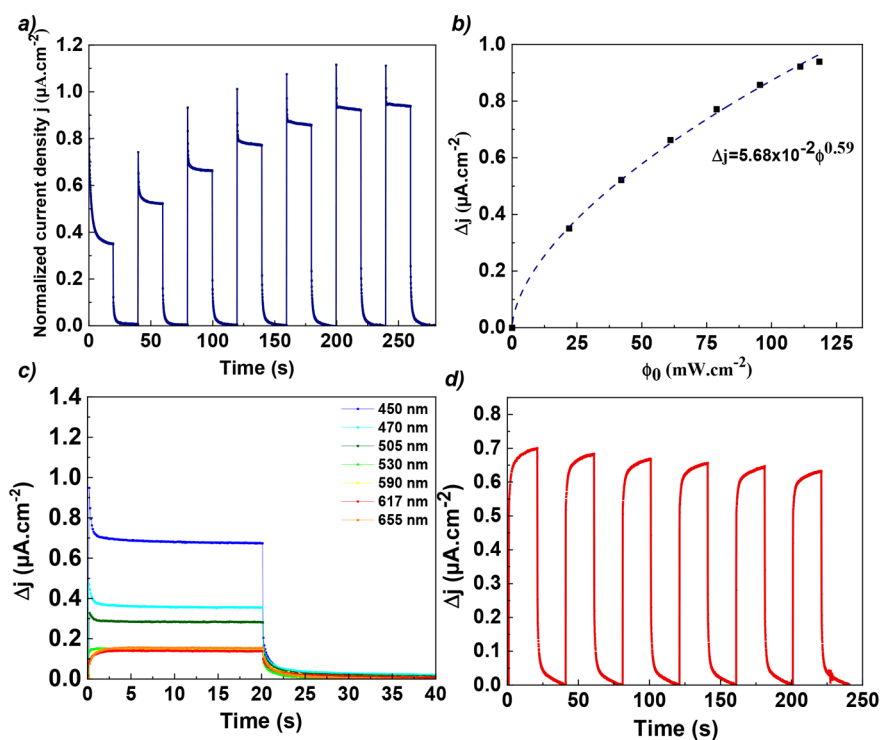


**Figure 7.** (a) Transient photocurrent response ( $V_{\text{bias}} = 0.4$  V under 450 nm excitation) of  $\text{Sr}_2\text{Sb}_2\text{O}_2\text{Se}_3$ . (b) Evolution of the photocurrent density the power density of light. (c) Transient photocurrent response vs wavelengths (constant light intensity  $\phi_0 = 38$   $\text{mW cm}^{-2}$ ) of  $\text{Sr}_2\text{Sb}_2\text{O}_2\text{Se}_3$ . (d) Transient photocurrent response under solar illumination ( $100$   $\text{mW cm}^{-2}$ ) for  $V_{\text{bias}} = 0.4$  V.

when a 0.4 V bias voltage was applied (see the [Supporting Information](#)).

The photoelectrode was then submitted to solar irradiation (150 W xenon lamp with an AM 1.5 G filter,  $-100$   $\text{mW cm}^{-2}$ ) and the transient photocurrent response was recorded under

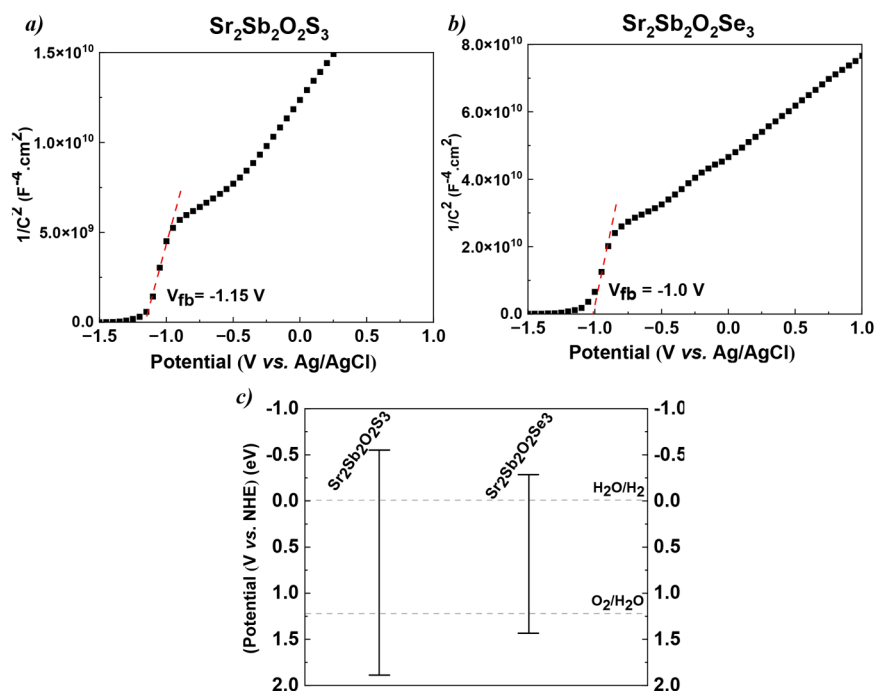


**Figure 8.** (a) Mott–Schottky plot for  $\text{Sr}_2\text{Sb}_2\text{O}_2\text{S}_3$  deposited on ITO/glass recorded at 100 Hz. (b) Mott–Schottky plot for  $\text{Sr}_2\text{Sb}_2\text{O}_2\text{Se}_3$  deposited on ITO/glass recorded at 1 kHz. (c) Calculated band edges positions for  $\text{Sr}_2\text{Sb}_2\text{O}_2\text{S}_3$  and  $\text{Sr}_2\text{Sb}_2\text{O}_2\text{Se}_3$ . The levels of  $\text{H}_2$  and  $\text{O}_2$  evolution are indicated by dashed lines.

different on/off cycles for two bias voltages, 0 and 0.4 V. **Figure 6d**, shows the response recorded for 0 V bias voltage: a photocurrent of  $3.2 \times 10^{-1} \mu\text{A}\cdot\text{cm}^{-2}$  is obtained with a slight decrease in the value upon increasing the power density, until stability at the end with a  $2.7 \times 10^{-1} \mu\text{A}\cdot\text{cm}^{-2}$  value. The response for a 0.4 V potential was also measured (**Supporting Information**) and gave a higher photocurrent ( $1.60 \mu\text{A}\cdot\text{cm}^{-2}$ ) but with a clear decrease ( $1.15 \mu\text{A}\cdot\text{cm}^{-2}$ ) at higher power densities. This behavior indicates the presence of progressive corrosion within the thick film in the chosen electrolyte, which may be accentuated by the applied potential. This was also observed after photocatalysis measurements, and XRPD analysis of the samples after photocurrent measurements (see below) would be useful to investigate this further. Although photocorrosion may occur upon the application of a potential in this material, its capacity to generate a photocurrent under sunlight without potential is rarely observed for this family of materials. For instance,  $[(\text{Ba}_{19}\text{Cl}_4)(\text{Ga}_6\text{Si}_{12}\text{O}_{42}\text{S}_8)]$  generates a transient photocurrent response when subjected to ultraviolet light excitation,<sup>70</sup> and the  $\text{LaGaS}_2\text{O}$  electrode produces an anodic photocurrent only under UV light.<sup>71</sup> The difference between the responses recorded under sunlight with both potentials (0.4 and 0 V) is consistent with the reproducibility test under 450 nm excitation and could be explained by the presence of some kind of photocorrosion when applying a potential, which is caused by the materials' instability in the used electrolyte. This hypothesis still needs to be studied and verified by further tests, including testing other electrolytes.

The photocurrent responses of the previously reported  $\text{Sr}_2\text{Sb}_2\text{O}_2\text{Se}_3$  were also measured with a 0.4 V bias voltage and under excitation of 450 nm (**Figure 7**). A linear increase in the transient photocurrent was observed under different illumination and dark cycles from 0.8 to  $1.1 \mu\text{A}\cdot\text{cm}^{-2}$  for a power density from 22 to  $111 \text{ mW}\cdot\text{cm}^{-2}$  (**Figure 7a**). As for

the oxysulfide, the generated photocurrent increased with the intensity of the luminous flux according to a classical power law<sup>67</sup> (**Figure 7b**), giving a curve going through the origin with an equation of  $\Delta j = (6.17 \times 10^{-2})\Phi^{0.58}$ . In  $\text{Sr}_2\text{Sb}_2\text{O}_2\text{Se}_3$ , the exponent value (0.58) is low, indicating the presence of many traps (although fewer than  $\text{Sr}_2\text{Sb}_2\text{O}_2\text{S}_3$  with exponents of 0.25 and 0.18 for 0 and 0.4 V, respectively). Unlike the oxysulfide, the photocurrent responses registered for  $\text{Sr}_2\text{Sb}_2\text{O}_2\text{Se}_3$  for 0.4 V (**Figure 7a**) and 0 V (**Supporting Information**) show the characteristic decay from a “spike”, indicating the presence of a competition between two phenomena (transfer and recombination). This can be explained by the rapid separation of the electron–hole pairs under illumination and then the establishment of an equilibrium state between the recombination and the transfer of the carriers. In fact, at 0.4 V the photocurrent peak is more square and shorter than that observed at 0 V, indicating more ideal behavior at 0.4 V, as the equilibrium is reached faster (giving a more square peak) and minimal recombination occurs (shorter peak). We can also note that without an applied potential the photocurrent generated tends toward a saturation value from  $42 \text{ mW}\cdot\text{cm}^{-2}$  (**Supporting Information**), while at  $V_{\text{bias}} = 0.4 \text{ V}$  we observe classical power law behavior (**Figure 7b**) without reaching saturation. To understand this behavior, it is possible in the case of a “spike” to calculate the transfer and recombination constants according to a model proposed by Parkinson et al.<sup>72</sup> In this model, the time constant of the decay is given by eq 2 as follows:

$$\frac{j(t) - j(\infty)}{j(0) - j(\infty)} = e^{-t/\tau} \quad \text{with } \tau = \frac{1}{k_{\text{rec}} + k_{\text{tr}}} \quad (2)$$

where  $\tau$ ,  $k_{\text{rec}}$ , and  $k_{\text{tr}}$  are the time constant, the recombination rate constant, and the transfer rate constant, respectively.



Moreover, the ratio of the steady state photocurrent to the instantaneous photocurrent observed when the illumination is switched on is given by eq 3 as follows:<sup>73</sup>

$$\frac{j(\infty)}{j(0)} = \frac{k_{\text{tr}}}{k_{\text{tr}} + k_{\text{rec}}} = \eta_{\text{tr}} \quad (3)$$

These two expressions make it possible to calculate the values of  $k_{\text{tr}}$ ,  $k_{\text{rec}}$ , and  $\eta_{\text{tr}}$  (transfer efficacy). This model was applied to extract the values of  $k_{\text{tr}}$  and  $k_{\text{rec}}$  as a function of light intensity for  $V_{\text{bias}} = 0$  and 0.4 V (Supporting Information). At  $118 \text{ mW}\cdot\text{cm}^{-2}$ , the rate constants at 0.4 V are  $k_{\text{tr}} = 7 \text{ min}^{-1}$  and  $k_{\text{rec}} = 1.5 \text{ min}^{-1}$  (i.e., a transfer efficiency of 85%, Supporting Information), and  $k_{\text{tr}} = 0.1 \text{ min}^{-1}$  and  $k_{\text{rec}} = 1.3 \text{ min}^{-1}$  (i.e., a transfer efficiency of 10%, Supporting Information) at 0 V.

The dependence of the photocurrent on the wavelengths recorded for 0.4 V bias voltage is shown in Figure 7c for  $\text{Sr}_2\text{Sb}_2\text{O}_2\text{Se}_3$ , and it shows a similar response to that recorded for the oxysulfide analogue (Supporting Information). The best efficiency was seen for 450 nm excitation with the highest photocurrent value of  $1.95 \mu\text{A}\cdot\text{cm}^{-2}$  and that decreases proportionally toward longer wavelengths. However, a significant photocurrent is observed over the entire spectral range (450 to 655 nm) unlike the oxysulfide, where the photocurrent drops drastically from 590 nm. To finish, the photoelectrode was exposed to solar irradiation (Figure 7d), which showed the good reproducibility of the photocurrent produced during the on/off cycles with only a very slight decrease. This result shows better photostability of the oxyselenide compared with its sulfur-based analogue.

The last electrochemical measurement performed for both compounds was a Mott–Schottky test: the (MS) plot of  $1/C^2$  vs the applied potential shown in Figure 8a and b indicates the conduction type, the concentration of the charge carriers ( $N$ ) and the flat-band potential ( $E_{\text{fb}}$ ).<sup>74</sup> The positive gradient in the Mott–Schottky plot of  $1/C^2$  vs  $V$  for  $\text{Sr}_2\text{Sb}_2\text{O}_2\text{S}_3$  is consistent with n-type semiconducting behavior, with a flat-band potential  $E_{\text{fb}}$  of  $-1.15 \text{ V}$  vs. Ag/AgCl (reference electrode) or  $-0.625 \text{ V}$  vs. RHE (reversible hydrogen electrode).<sup>75</sup> Indeed, a potential measured with respect to Ag/AgCl ( $E_{\text{Ag/AgCl}}$ ) can be converted to the RHE scale ( $E_{\text{RHE}}$ ) with eq 4 as follows:

$$E_{\text{RHE}} = E_{\text{Ag/AgCl}} + E_{\text{Ag/AgCl}}^0 + 0.059\text{pH} \quad (4)$$

where  $E_{\text{Ag/AgCl}}^0$  is the potential of the Ag/AgCl reference electrode with respect to the standard hydrogen electrode (SHE) fixed at 195 mV. The pH of 0.1 M  $\text{Na}_2\text{SO}_4$  electrolyte is 5.6.

The Mott–Schottky plot for  $\text{Sr}_2\text{Sb}_2\text{O}_2\text{Se}_3$  (Figure 8b) is also consistent with n-type semiconducting behavior, with a flat-band potential  $E_{\text{fb}}$  of  $-1.0 \text{ V}$  vs. Ag/AgCl (reference electrode) or  $-0.475 \text{ V}$  vs. RHE (reversible hydrogen electrode).

Depending on the conduction type, the flat-band potential serves to locate the valence and conduction band edge positions<sup>75</sup> because it reflects the position of the Fermi level, which lies at 0.1 V lower than the conduction band for the n-type semiconductors.<sup>76–78</sup> Therefore, this calculated value is close to the calculated CB band edge position (Figure 8c) using the empirical method based on Mulliken electro-negativities proposed by Butler and Ginley<sup>79</sup> and further described by Xu and Schoonen<sup>80</sup> using the following equation:

$$E_{\text{VB,CB}} = E_0 + \prod_{M=1}^n \chi_M^{j^{1/n}} \pm \frac{E_{\text{gap}}}{2} \quad (5)$$

where  $E_{\text{VB,CB}}$  corresponds to the positions of the valence and conduction band edges,  $E_0$  corresponds to the difference between NHE and the vacuum ( $E_0 = -4.5 \text{ eV}$ ),  $\chi_M$  is the electronegativity of the atom  $M$  in the Mulliken scale with  $n$  the number of atoms, and  $j$  the stoichiometric ratio. Such calculations for the band edge positions were reported in a study by Castelli et al.,<sup>81</sup> which compares a number of photocatalysts. Our calculations using this method confirm that the band edges for  $\text{Sr}_2\text{Sb}_2\text{O}_2\text{S}_3$  and  $\text{Sr}_2\text{Sb}_2\text{O}_2\text{Se}_3$  are appropriate for the redox potential of water and are consistent with the edge positions determined experimentally from Mott–Schottky measurements and the optical band gaps.

**Photocatalytic Activity.** UV–vis spectroscopy was used to follow the kinetics of the photodegradation of rhodamine B based on the maximum absorption, allowing the photocatalytic efficiency of  $\text{Sr}_2\text{Sb}_2\text{O}_2\text{Q}_3$  ( $Q = \text{S}, \text{Se}$ ) phases to be quantified. The photocatalytic kinetics at the solid–liquid interface were described using the Langmuir–Hinshelwood model (LH),<sup>82</sup> taking an order of one for the photodegradation reaction and plotting  $\ln(C_0/C)$  vs time to determine the apparent rate constant ( $k_{\text{app}}$ ). Figure 9 shows the corresponding kinetic plots

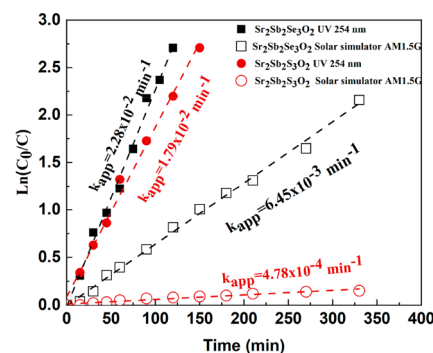


**Figure 9.** Langmuir–Hinshelwood kinetic plot for the degradation of rhodamine B on  $\text{Sr}_2\text{Sb}_2\text{O}_2\text{Q}_3$  ( $Q = \text{S}, \text{Se}$ ) under UV (254 nm, 40 W) and solar ( $100 \text{ mW}\cdot\text{cm}^{-2}$ ) irradiation.

for  $\text{Sr}_2\text{Sb}_2\text{O}_2\text{Q}_3$  ( $Q = \text{S}, \text{Se}$ ) photocatalysts under UV and solar irradiation. Under UV light, both photocatalysts exhibited similar efficiency, where a linear evolution occurred with apparent rate constants of  $2.28 \times 10^{-2}$  and  $1.79 \times 10^{-2} \text{ min}^{-1}$  for  $\text{Sr}_2\text{Sb}_2\text{O}_2\text{Se}_3$  and  $\text{Sr}_2\text{Sb}_2\text{O}_2\text{S}_3$ , respectively. These results reveal good kinetic performance for both phases and are comparable with those of other photocatalysts (typically  $10^{-2} \text{ min}^{-1}$ ), such as  $\text{La}_2\text{Ti}_2\text{O}_7$  oxide<sup>74</sup> and  $\text{Sr}_6\text{Cd}_2\text{Sb}_6\text{S}_{10}\text{O}_7$  oxysulfide.<sup>20</sup> The performance of both materials decreased under solar irradiation, but it is striking that quite significant activity was still observed for  $\text{Sr}_2\text{Sb}_2\text{O}_2\text{Se}_3$  (with rate constant  $6.45 \times 10^{-3} \text{ min}^{-1}$ ). It should be noted that it is difficult to disperse the  $\text{Sr}_2\text{Sb}_2\text{O}_2\text{S}_3$  phase in solution, and 20 min of sonication was needed to break up agglomerates and give the best photocatalytic efficiency.  $\text{Sr}_2\text{Sb}_2\text{O}_2\text{Se}_3$  showed better dispersion (less sonication was needed), and the maximum efficiency is reached more quickly. The kinetics of the photodegradation reaction is usually influenced by the microstructure and the morphology of the photocatalyst as well as its stability in the chosen electrolyte; nonetheless, structural parameters (such as polarity and lone pairs) can also

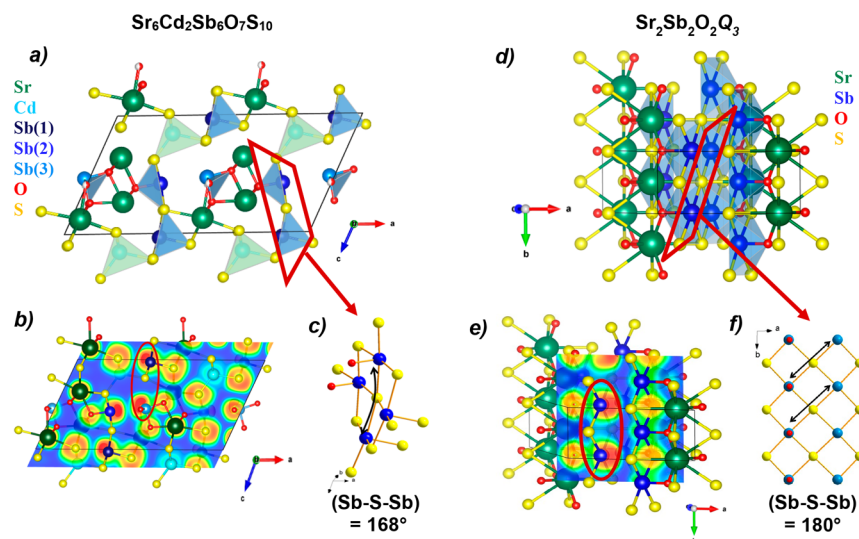


**Figure 10.** (a and d) Representations of the structures of the  $\text{Sr}_6\text{Cd}_2\text{Sb}_6\text{O}_7\text{S}_{10}$  and  $\text{Sr}_2\text{Sb}_2\text{O}_2\text{Q}_3$  phases, respectively. (b and e) Orbital overlap due to the distance between Sb 5s pairs in  $\text{Sr}_6\text{Cd}_2\text{Sb}_6\text{O}_7\text{S}_{10}$  and  $\text{Sr}_2\text{Sb}_2\text{O}_2\text{Q}_3$ , respectively. (c and f) View showing a curvature due to deviation of the Sb–S–Sb angle from  $168^\circ$  in  $\text{Sr}_6\text{Cd}_2\text{Sb}_6\text{O}_7\text{S}_{10}$  to  $180^\circ$  in  $\text{Sr}_2\text{Sb}_2\text{O}_2\text{Q}_3$ , respectively.

influence the outcome of the reaction. The photocatalytic efficiency of  $\text{Sr}_2\text{Sb}_2\text{O}_2\text{Q}_3$  under solar light ( $k = 4.78 \times 10^{-4}$  and  $6.45 \times 10^{-3} \text{ min}^{-1}$  for S and Se, respectively) is comparable to that of copper oxysulfide BiCuSO ( $k = 9.1 \times 10^{-3} \text{ min}^{-1}$ ), which is capable of degrading an organic pollutant (Congo Red) in aqueous solution under visible light.<sup>83</sup>

Unfortunately, based on the previous photoelectrochemical studies, significant photocorrosion was observed for  $\text{Sr}_2\text{Sb}_2\text{O}_2\text{S}_3$  upon applying a bias voltage (Figures 6 d and Supporting Information). XRPD patterns of the powder before and after the catalysis and the electrochemical and unit cell parameter measurements (Supporting Information) do not show any major differences, but slight peak broadening might indicate sample degradation and lower crystallinity of the samples after catalysis.

SEM analysis was also carried out on the after-test samples to investigate the grain size and shape (Supporting Information) and indicated that the crystallite size remains comparable. Therefore, photocorrosion cannot be attributed to a structural change but rather to a progressive deterioration (dissolution) of the photoelectrode in the electrolyte. Future work to optimize the electrolyte and film stability would be worthwhile.

## DISCUSSION

The new oxysulfide  $\text{Sr}_2\text{O}_2\text{Sb}_2\text{S}_3$  described here adopts a crystal structure very similar to that of its oxyselenide analogue  $\text{Sr}_2\text{O}_2\text{Sb}_2\text{Se}_3$  reported by Panella et al.<sup>35</sup> A key structural feature in several  $\text{Sb}^{3+}$  oxychalcogenides is the one-dimensional (1D) chains of edge-linked  $\text{SbOS}_4$  square-based pyramids. In the  $\text{Sr}_2\text{O}_2\text{Sb}_2\text{Q}_3$  phases discussed here, these form double chains of  ${}^1_{\infty}[\text{Sb}_2\text{O}_2\text{S}_{2.5}]^{-3}$  which extend along the [010] direction. In the more complex  $\text{Sr}_6\text{Cd}_2\text{Sb}_6\text{Q}_{10}\text{O}_7$  ( $\text{Q} = \text{S}, \text{Se}$ ) materials,<sup>20,19</sup> single chains of  $\text{SbOS}_4$  units are edge-linked with  $\text{SbS}_5$  chains to form double-chains of  ${}^1_{\infty}[\text{Sb}_2\text{OS}_{3.5}]^{-3}$  corner linked to  ${}^1_{\infty}[\text{CdS}_3]^{4-}$  chains, and with isolated  ${}^1_{\infty}[\text{SbO}_{2.5}]^{2-}$  chains also in the structure. These structural features have a direct impact on electron and hole mobilities and, therefore, on the photocurrent response and photocatalytic activity.

These three antimony oxychalcogenides have low  $m_h^*$  values (0.163, 0.191, and 0.215 for  $\text{Sr}_2\text{O}_2\text{Sb}_2\text{Se}_3$ ,  $\text{Sr}_2\text{O}_2\text{Sb}_2\text{S}_3$  and  $\text{Sr}_6\text{Cd}_2\text{Sb}_6\text{S}_{10}\text{O}_7$ ,<sup>20</sup> respectively) and hence high mobilities within Sb–S planes, undoubtedly influenced by the effective overlap of Sb 5p and S 3p/Se 4p orbitals that make up the bottom of the conduction band. The Sb–Q–Sb angles are constrained by symmetry to be  $180^\circ$  in  $\text{Sr}_2\text{O}_2\text{Sb}_2\text{Q}_3$ , while the double chains in  $\text{Sr}_6\text{Cd}_2\text{Sb}_6\text{S}_{10}\text{O}_7$  are curved and have Sb–S–Sb angles of  $\sim 168^\circ$ , (Figure 10) decreasing the orbital overlap and bandwidth. In  $\text{Sr}_2\text{O}_2\text{Sb}_2\text{Q}_3$ , the  $\text{SbOQ}_4$  units within the double-chains are arranged in an anti-fashion, and the increased stereochemical activity of the  $\text{Sb}^{3+} 5s^2$  pair for the oxysulfide (Table 2) gives a slightly greater distortion of the  $\text{SbOS}_4$  square-based pyramids (giving basal-plane S–Sb–S angles of  $\sim 171^\circ$ , compared with Se–Sb–Se angles of  $\sim 174^\circ$ ).

The striking difference between these oxychalcogenides is in their hole effective masses with extremely low  $m_h^*$  for  $\text{Sr}_2\text{O}_2\text{Sb}_2\text{Se}_3$  (Table 1). Theory studies on  $\text{Sn}^{2+}$  oxides highlight the impact of the extent and direction of orbital overlap between  $\text{Sn}^{2+} 5s$  and O 2p orbitals on the curvature of the conduction band and hence the hole mobility.<sup>84</sup> Ha et al. highlight the importance of Sn–O–Sn angles close to  $180^\circ$  to optimize this hybridization<sup>84</sup> and the greater deviation from  $180^\circ$  for Sb–S–Sb angles in  $\text{Sr}_6\text{Cd}_2\text{Sb}_6\text{S}_{10}\text{O}_7$  ( $168^\circ$ ) will be detrimental for this mixing. The VBMs in  $\text{Sr}_2\text{O}_2\text{Sb}_2\text{Q}_3$  and in  $\text{Sr}_6\text{Cd}_2\text{Sb}_6\text{S}_{10}\text{O}_7$  are composed of the Sb 5s and S/Se  $np$  states, with the relative energies of these orbitals also determining the degree of stereochemical activity of the Sb  $5s^2$  electron pair. Overlap between  $\text{SbS}_5$  and  $\text{SbOS}_4$  lone pairs in  $\text{Sr}_6\text{Cd}_2\text{Sb}_6\text{S}_{10}\text{O}_7$  is hampered by their huge separation in the crystal structure along the direction of the stereochemically active pairs (see Figure 10), giving rise to a very high hole effective mass ( $m_h^* = 6.5 m_0$ ). By contrast, the Sb  $5s^2$  pairs in  $\text{Sr}_2\text{O}_2\text{Sb}_2\text{Q}_3$  are separated by only  $\sim 4 \text{ \AA}$  along the direction close to the orientation of both electron pairs ( $\Gamma \rightarrow \text{B}$ ). This leads to exceptionally low  $m_h^*$  values for  $\text{Sr}_2\text{O}_2\text{Sb}_2\text{Se}_3$ , making it particularly attractive for efficient photoconduction and photocatalysis applications. It would be interesting to carry out conductivity measurements as a function of temperature to

allow comparison with other high-mobility materials (e.g., the p-type oxysulfide  $\text{Cu}_2\text{S}_2\text{Sr}_3\text{Sc}_2\text{O}_5$ ).<sup>85</sup>

The reduced optical band gap of the oxyselenide compared with the oxysulfide (from diffuse reflectance measurements, Figure 3) is consistent with our electronic structure calculations (Figure 4), which revealed a more dispersed conduction band (composed largely of Se 4p states) compared with the oxysulfide analogue.

Upon heating in Ar(g),  $\text{Sr}_2\text{O}_2\text{Sb}_2\text{S}_3$  decomposes, releasing SO (as determined by mass spectrometry). XRPD of the decomposition products (or in situ studies) are needed to confirm the nature of this decomposition, but the reducing atmosphere could favor reduction to metallic antimony and formation of oxides and sulfides of strontium (e.g.,  $\text{Sr}_2\text{O}_2\text{Sb}_2\text{S}_3 \rightarrow \text{SrO}(s) + \text{SrS}_2(s) + 2\text{Sb}(s) + \text{SO}(g)$ ).

In terms of the photocurrent response and photocatalytic activity, the results reported here for  $\text{Sr}_2\text{Sb}_2\text{O}_2\text{Q}_3$  (Q = S, Se) oxychalcogenides reveal their capacity to exhibit photoelectric activity. Their potential to generate a reproducible photocurrent with no applied potential under solar irradiation is striking and makes them promising candidates for photocatalysis in the visible range. This behavior might result from the presence of polar coordination environments within the structure (dipoles across  $[\text{SbOSe}_4]^{7-}$  and  $[\text{SbOS}_4]^{7-}$  units are 15 and 15.5 D, respectively),<sup>55,19</sup> which makes it possible for the charge carriers to separate without applying an external electric field. In fact, it has been previously reported that introducing polar units, with a built-in electric field, can enhance the electron–hole separation in the photocatalytic material<sup>186–88</sup> by facilitating the transfer of the photogenerated pairs to different active sites,<sup>89</sup> resulting in a better photoactivity.<sup>90</sup> Recently, similar results were observed for the  $\text{Sr}_6\text{Cd}_2\text{Sb}_6\text{O}_7\text{Q}_{10}$  (Q = S, Se) polar oxysulfide<sup>19,20</sup> and the  $\text{Na}_3\text{VO}_2\text{B}_6\text{O}_{11}$  polar oxide.<sup>91</sup>

The different peak shapes observed in the photocurrent measurements for  $\text{Sr}_2\text{Sb}_2\text{O}_2\text{S}_3$  and  $\text{Sr}_2\text{Sb}_2\text{O}_2\text{Se}_3$  (Figures 6a and 7a) indicate that the charge carriers separate faster upon illumination in the case of the oxyselenide (with spiky peaks), while slower separation occurs in the case of the oxysulfide. This is related to the lower effective masses for the oxyselenide, reflecting its more covalent nature. Lower effective masses will allow faster mobility, therefore making it more probable that the charge carriers reach the surface before recombination.

## CONCLUSION

The potential of  $\text{Sr}_2\text{Sb}_2\text{O}_2\text{Q}_3$  (Q = S, Se) oxychalcogenides for photocatalytic activity is highlighted in this work. These materials may be promising candidates as photocatalysts for water splitting under UV and solar irradiation. Several aspects contributed to this activity, including the presence of a stereochemically active lone pair (Sb 5s<sup>2</sup>) and a mixed-anion environment (O/S or Se). The nature of the chalcogenide can tune both the magnitude of the band gap (Figure 3) and the effective masses for both the electrons and holes. The exceptionally low hole effective mass for  $\text{Sr}_2\text{Sb}_2\text{O}_2\text{Se}_3$  can be attributed to the presence of the highly covalent selenide ion (Sb 5s–Se 4p hybridization). Both  $\text{Sr}_2\text{Sb}_2\text{O}_2\text{Q}_3$  (Q = S, Se) materials gave photocurrent responses under solar irradiation with no applied external bias voltage, highlighting the importance of intrinsic polarization within the structure. More efficient electron–hole separation and migration were observed for  $\text{Sr}_2\text{Sb}_2\text{O}_2\text{Se}_3$ , which is explained by the lower effective masses calculated for this oxyselenide (attributed to

its more covalent nature). These two antimony oxychalcogenides showed photocatalytic activity, degrading rhodamine B under solar light. This study illustrates the importance of Sb<sup>3+</sup> oxychalcogenides for photocatalytic and photocurrent applications as a result of their tunable band gap, stereochemically active 5s<sup>2</sup> electron pair, and resulting high electron and hole mobilities.

## ASSOCIATED CONTENT

### Supporting Information

The Supporting Information is available free of charge at <https://pubs.acs.org/doi/10.1021/acs.chemmater.3c01298>.

Rietveld refinement details of  $\text{Sr}_2\text{Sb}_2\text{O}_2\text{Q}_3$  using room temperature XRPD data, electron microscopy analysis details on  $\text{Sr}_2\text{Sb}_2\text{O}_2\text{Q}_3$ , electronic structure and density of states in the  $C2/m$  model and additional plots of the fat bands and stereochemical activity in the  $P2_1/c$  model, additional photocurrent and photocatalysis measurements, and optimized structure parameters and atomic positions for  $\text{Sr}_2\text{Sb}_2\text{O}_2\text{Q}_3$  in both  $P2_1/c$  and  $C2/m$  space groups (PDF)

CIF for SI Table 1 (CIF)

CIF for SI Table 2 (CIF)

CIF for SI Table 3 (CIF)

CIF for SI Table 4 (CIF)

## AUTHOR INFORMATION

### Corresponding Authors

Emma E. McCabe – *Department of Physics, Durham University, Durham DH1 3LE, U.K.*; [orcid.org/0000-0001-5868-4570](https://orcid.org/0000-0001-5868-4570); Email: [emma.mccabe@durham.ac.uk](mailto:emma.mccabe@durham.ac.uk)

Houria Kabbour – *University of Lille, CNRS, Centrale Lille, ENSCL, University of Artois, UMR 8181 Unité de Catalyse et Chimie du Solide (UCCS), F-59000 Lille, France; Institut des Matériaux de Nantes Jean Rouxel, Nantes Université, CNRS, 44000 Nantes, France*; [orcid.org/0000-0002-9081-3261](https://orcid.org/0000-0002-9081-3261); Email: [houria.kabbour@cnrs-immn.fr](mailto:houria.kabbour@cnrs-immn.fr)

### Authors

Sandy Al Bacha – *University of Lille, CNRS, Centrale Lille, ENSCL, University of Artois, UMR 8181 Unité de Catalyse et Chimie du Solide (UCCS), F-59000 Lille, France; School of Physical Sciences, University of Kent, Canterbury, Kent CT2 7NH, U.K.; Department of Physics, Durham University, Durham DH1 3LE, U.K.*

Sébastien Saitzek – *University of Artois, CNRS, Centrale Lille, University of Lille, UMR 8181, Unité de Catalyse et Chimie du Solide (UCCS), F-62300 Lens, France*; [orcid.org/0000-0003-1403-5397](https://orcid.org/0000-0003-1403-5397)

Pascal Roussel – *University of Lille, CNRS, Centrale Lille, ENSCL, University of Artois, UMR 8181 Unité de Catalyse et Chimie du Solide (UCCS), F-59000 Lille, France*; [orcid.org/0000-0001-7243-7293](https://orcid.org/0000-0001-7243-7293)

Marielle Huvé – *University of Lille, CNRS, Centrale Lille, ENSCL, University of Artois, UMR 8181 Unité de Catalyse et Chimie du Solide (UCCS), F-59000 Lille, France*

Complete contact information is available at:

<https://pubs.acs.org/doi/10.1021/acs.chemmater.3c01298>

### Notes

The authors declare no competing financial interest.



## ACKNOWLEDGMENTS

I-Site (ULNE), University of Lille, and University of Kent are thanked for cotutelle funding (S.A.B.). Durham University is thanked for hosting a research visit. Dr. Donna Arnold is thanked for helpful discussions. This study was supported by the French government through the Programme Investissement d'Avenir (I-SITE ULNE/ANR-16-IDEX-0004 ULNE) managed by the Agence Nationale de la Recherche (project ANION-COMBO). X-rays diffractometers are funded by Région NPDC, FEDER, CNRS, and MESR. The regional computational cluster supported by Lille University, CPER Nord-Pas-de-Calais/CRDER, France Grille CNRS, and FEDER is thanked for providing computational resources. The Chevreur Institute is thanked for its help in the development of this work through the ARCHI-CM project supported by the "Ministère de l'Enseignement Supérieur de la Recherche et de l'Innovation", the region "Hauts-de-France", and the ERDF program of the European Union and the "Métropole Européenne de Lille".

## REFERENCES

- (1) Wachsmann, E. D.; Lee, K. T. Lowering the Temperature of Solid Oxide Fuel Cells. *Science* **2011**, *334* (6058), 935–939.
- (2) Kong, D.; Zheng, Y.; Kobielski, M.; Wang, Y.; Bai, Z.; Macyk, W.; Wang, X.; Tang, J. Recent Advances in Visible Light-Driven Water Oxidation and Reduction in Suspension Systems. *Mater. Today* **2018**, *21* (8), 897–924.
- (3) Ikeda, S.; Hara, M.; Kondo, J. N.; Domen, K.; Takahashi, H.; Okubo, T.; Kakihana, M. Preparation of a High Active Photocatalyst, K<sub>2</sub>La<sub>2</sub>Ti<sub>3</sub>O<sub>10</sub>, by Polymerized Complex Method and Its Photocatalytic Activity of Water Splitting. *Journal of materials research* **1998**, *13* (4), 852–855.
- (4) Belver, C.; Adán, C.; Fernández-García, M. Photocatalytic Behaviour of Bi<sub>2</sub>MO<sub>6</sub> Polymetalates for Rhodamine B Degradation. *Catal. Today* **2009**, *143* (3), 274–281.
- (5) Hashimoto, K.; Irie, H.; Fujishima, A. TiO<sub>2</sub> Photocatalysis: A Historical Overview and Future Prospects. *Japanese journal of applied physics* **2005**, *44* (12R), 8269.
- (6) Maruska, H. P.; Ghosh, A. K. Photocatalytic Decomposition of Water at Semiconductor Electrodes. *Sol. Energy* **1978**, *20* (6), 443–458.
- (7) Van Benthem, K.; Elsässer, C.; French, R. Bulk Electronic Structure of SrTiO<sub>3</sub>: Experiment and Theory. *Journal of applied physics* **2001**, *90* (12), 6156–6164.
- (8) Ji, S. M.; Choi, S. H.; Jang, J. S.; Kim, E. S.; Lee, J. S. Band Gap Tailored Zn (Nb<sub>1-x</sub>V<sub>x</sub>)<sub>2</sub>O<sub>6</sub> Solid Solutions as Visible Light Photocatalysts. *J. Phys. Chem. C* **2009**, *113* (41), 17824–17830.
- (9) Subramanian, Y.; Dhanasekaran, A.; Omeiza, L. A.; Somalu, M. R.; Azad, A. K. A Review on Heteroanionic-Based Materials for Photocatalysis Applications. *Catalysts* **2023**, *13* (1), 173.
- (10) Yadav, G.; Ahmaruzzaman, M. Multi Anion-Based Materials: Synthesis and Catalytic Applications. *Mater. Res. Bull.* **2022**, *152*, 111836.
- (11) Katori, H. A.; Adachi, T.; Ohta, H.; Nakamura, S.; Fuwa, A. Magnetism in Two-Leg Ladder Compound Ba<sub>6</sub>Fe<sub>8</sub>S<sub>15</sub> with Mixed Oxidation State of Iron. *Physics Procedia* **2015**, *75*, 552–556.
- (12) Almoussawi, B.; Tomohiri, H.; Kageyama, H.; Kabbour, H. High Pressure Synthesis of the Spin Chain Sulfide Ba<sub>9</sub>V<sub>3</sub>S<sub>11</sub>(S<sub>2</sub>)<sub>2</sub>. *Eur. J. Inorg. Chem.* **2021**, *2021* (13), 1271–1277.
- (13) Jia, Y.; Yang, J.; Zhao, D.; Han, H.; Li, C. A Novel Sr<sub>2</sub>CuInO<sub>3</sub>S P-Type Semiconductor Photocatalyst for Hydrogen Production under Visible Light Irradiation. *Journal of energy chemistry* **2014**, *23* (4), 420–426.
- (14) Hyett, G.; Limburn, G. J.; Iborra Torres, A.; Scanlon, D. O.; Williamson, B.; Stephens, M. Photocatalytic, Structural and Optical Properties of Mixed Anion Solid Solutions Ba<sub>3</sub>Sc<sub>2</sub>XIn<sub>x</sub>O<sub>5</sub>Cu<sub>2</sub>S<sub>2</sub> and Ba<sub>3</sub>In<sub>2</sub>O<sub>5</sub>Cu<sub>2</sub>S<sub>2</sub>-YSey. *Journal of Materials Chemistry A* **2020**, *8*, 19887–19897.
- (15) Vonrüti, N. *Ferroelectricity and Metastability in (Mixed-Anion) Perovskite Oxides for Improved Solar Water Splitting*. Ph.D. Dissertation, University of Bern: Bern, Switzerland, 2019.
- (16) Clarke, S. J.; Adamson, P.; Herkelrath, S. J.; Rutt, O. J.; Parker, D. R.; Pitcher, M. J.; Smura, C. F. Structures, Physical Properties, and Chemistry of Layered Oxychalcogenides and Oxypnictides. *Inorganic chemistry* **2008**, *47* (19), 8473–8486.
- (17) Ueda, K.; Hiramatsu, H.; Hirano, M.; Kamiya, T.; Hosono, H. Wide-Gap Layered Oxychalcogenide Semiconductors: Materials, Electronic Structures and Optoelectronic Properties. *Thin Solid Films* **2006**, *496* (1), 8–15.
- (18) Vonrüti, N.; Aschauer, U. Band-Gap Engineering in AB (O x S 1-x) Perovskite Oxysulfides: A Route to Strongly Polar Materials for Photocatalytic Water Splitting. *Journal of Materials Chemistry A* **2019**, *7* (26), 15741–15748.
- (19) Wang, R.; Wang, F.; Zhang, X.; Feng, X.; Zhao, C.; Bu, K.; Zhang, Z.; Zhai, T.; Huang, F. Improved Polarization in the Sr<sub>6</sub>Cd<sub>2</sub>Sb<sub>6</sub>O<sub>7</sub>Se<sub>10</sub> Oxyselenide through Design of Lateral Sublattices for Efficient Photoelectric Conversion. *Angew. Chem.* **2022**, *61*, e202206816.
- (20) Al Bacha, S.; Saitzek, S.; McCabe, E. E.; Kabbour, H. Photocatalytic and Photocurrent Responses to Visible Light of the Lone-Pair-Based Oxysulfide Sr<sub>6</sub>Cd<sub>2</sub>Sb<sub>6</sub>S<sub>10</sub>O<sub>7</sub>. *Inorg. Chem.* **2022**, *61* (46), 18611–18621.
- (21) Wang, Q.; Nakabayashi, M.; Hisatomi, T.; Sun, S.; Akiyama, S.; Wang, Z.; Pan, Z.; Xiao, X.; Watanabe, T.; Yamada, T.; et al. Oxysulfide Photocatalyst for Visible-Light-Driven Overall Water Splitting. *Nat. Mater.* **2019**, *18* (8), 827–832.
- (22) Miura, A.; Oshima, T.; Maeda, K.; Mizuguchi, Y.; Moriyoshi, C.; Kuroiwa, Y.; Meng, Y.; Wen, X.-D.; Nagao, M.; Higuchi, M.; et al. Synthesis, Structure and Photocatalytic Activity of Layered LaOInS<sub>2</sub>. *J. Mater. Chem. A* **2017**, *5* (27), 14270–14277.
- (23) Kabbour, H.; Sayede, A.; Saitzek, S.; Lefevre, G.; Cario, L.; Trentesaux, M.; Roussel, P. Structure of the Water-Splitting Photocatalyst Oxysulfide  $\alpha$ -LaOInS<sub>2</sub> and Ab Initio Prediction of New Polymorphs. *Chem. Commun.* **2020**, *56* (11), 1645–1648.
- (24) Medvedeva, J. E. Magnetically Mediated Transparent Conductors: In<sub>2</sub>O<sub>3</sub> Doped with Mo. *Physical review letters* **2006**, *97* (8), 086401.
- (25) Van Hest, M.; Dabney, M. S.; Perkins, J. D.; Ginley, D. S.; Taylor, M. P. Titanium-Doped Indium Oxide: A High-Mobility Transparent Conductor. *Appl. Phys. Lett.* **2005**, *87* (3), 032111.
- (26) Hautier, G.; Miglio, A.; Ceder, G.; Rignanese, G.-M.; Gonze, X. Identification and Design Principles of Low Hole Effective Mass P-Type Transparent Conducting Oxides. *Nat. Commun.* **2013**, *4*, 2292.
- (27) Medvedeva, J. E.; Hettiarachchi, C. L. Tuning the Properties of Complex Transparent Conducting Oxides: Role of Crystal Symmetry, Chemical Composition, and Carrier Generation. *Phys. Rev. B* **2010**, *81* (12), 125116.
- (28) Minami, T. Transparent and Conductive Multicomponent Oxide Films Prepared by Magnetron Sputtering. *Journal of Vacuum Science & Technology A: Vacuum, Surfaces, and Films* **1999**, *17* (4), 1765–1772.
- (29) Kamiya, T.; Hosono, H. Material Characteristics and Applications of Transparent Amorphous Oxide Semiconductors. *NPG Asia Materials* **2010**, *2* (1), 15–22.
- (30) Fortunato, E.; Barquinha, P.; Martins, R. Oxide Semiconductor Thin-film Transistors: A Review of Recent Advances. *Advanced materials* **2012**, *24* (22), 2945–2986.
- (31) Kawazoe, H.; Yanagi, H.; Ueda, K.; Hosono, H. Transparent P-Type Conducting Oxides: Design and Fabrication of Pn Heterojunctions. *MRS Bull.* **2000**, *25* (8), 28–36.
- (32) Kawazoe, H.; Yasukawa, M.; Hyodo, H.; Kurita, M.; Yanagi, H.; Hosono, H. P-Type Electrical Conduction in Transparent Thin Films of CuAlO<sub>2</sub>. *Nature* **1997**, *389* (6654), 939–942.
- (33) Kim, T.; Yoo, B.; Youn, Y.; Lee, M.; Song, A.; Chung, K.-B.; Han, S.; Jeong, J. K. Material Design of New P-Type Tin Oxyselenide



Semiconductor through Valence Band Engineering and Its Device Application. *ACS Appl. Mater. Interfaces* **2019**, *11* (43), 40214–40221.

(34) Arai, T.; Iimura, S.; Kim, J.; Toda, Y.; Ueda, S.; Hosono, H. Chemical Design and Example of Transparent Bipolar Semiconductors. *J. Am. Chem. Soc.* **2017**, *139* (47), 17175–17180.

(35) Panella, J. R.; Chamorro, J.; McQueen, T. M. Synthesis and Structure of Three New Oxychalcogenides:  $A_2O_2Bi_2Se_3$  ( $A = Sr, Ba$ ) and  $Sr_2O_2Sb_2Se_3$ . *Chem. Mater.* **2016**, *28* (3), 890–895.

(36) Coelho, A. *TOPAS Academic: General Profile and Structure Analysis Software For Powder Diffraction Datafile*, ver. 5; Coelho Software: Brisbane, Australia, 2012.

(37) Coelho, A. A. TOPAS and TOPAS-Academic: An Optimization Program Integrating Computer Algebra and Crystallographic Objects Written in C++. *J. Appl. Crystallogr.* **2018**, *51* (1), 210–218.

(38) Dollase, W. A. Correction of Intensities for Preferred Orientation in Powder Diffraction: Application of the March Model. *J. Appl. Crystallogr.* **1986**, *19* (4), 267–272.

(39) Kresse, G.; Joubert, D. From Ultrasoft Pseudopotentials to the Projector Augmented-Wave Method. *Physical review b* **1999**, *59* (3), 1758.

(40) Blöchl, P. E. Projector Augmented-Wave Method. *Phys. Rev. B* **1994**, *50* (24), 17953.

(41) Sun, G.; Kürti, J.; Rajczyk, P.; Kertesz, M.; Hafner, J.; Kresse, G. Performance of the Vienna Ab Initio Simulation Package (VASP) in Chemical Applications. *Journal of Molecular Structure: THEOCHEM* **2003**, *624* (1–3), 37–45.

(42) Perdew, J. P.; Burke, K.; Ernzerhof, M. Generalized Gradient Approximation Made Simple. *Physical review letters* **1996**, *77* (18), 3865.

(43) Momma, K.; Izumi, F. VESTA 3 for three-dimensional visualization of crystal, volumetric and morphology data. *J. Appl. Cryst.* **2011**, *44*, 1272–1276.

(44) Maintz, S.; Deringer, V. L.; Tchougréeff, A. L.; Dronskowski, R. LOBSTER: A Tool to Extract Chemical Bonding from Plane-wave Based DFT. *J. Comput. Chem.* **2016**, *37*, 1030.

(45) Dronskowski, R.; Blochl, P. E. Crystal Orbital Hamilton Populations (COHP): Energy-Resolved Visualization of Chemical Bonding in Solids Based on Density-Functional Calculations. *J. Phys. Chem.* **1993**, *97* (33), 8617–8624.

(46) Deringer, V. L.; Tchougréeff, A. L.; Dronskowski, R. Crystal Orbital Hamilton Population (COHP) Analysis as Projected from Plane-Wave Basis Sets. *J. Phys. Chem. A* **2011**, *115* (21), 5461–5466.

(47) Mentré, O.; Juárez-Rosete, M. A.; Saitzek, S.; Aguilar-Maldonado, C.; Colmont, M.; Arévalo-López, A. M.  $S = 1/2$  Chain in  $BiVO_3F$ : Spin Dimers versus Photoanodic Properties. *J. Am. Chem. Soc.* **2021**, *143* (18), 6942–6951.

(48) Kubelka, P.; Munk, F. A Contribution to the Optics of Pigments. *Z. Technol. Phys.* **1931**, *12*, 593–601.

(49) Tauc, J.; Grigorovici, R.; Vancu, A. Optical Properties and Electronic Structure of Amorphous Germanium. *physica status solidi (b)* **1966**, *15* (2), 627–637.

(50) Jiang, S.; Liu, Y.; Xu, J. Rare Earth Oxynitrides: Promising Visible-Light-Driven Photocatalysts for Water Splitting. *Materials Advances* **2021**, *2* (4), 1190–1203.

(51) Siritanaratkul, B.; Maeda, K.; Hisatomi, T.; Domen, K. Synthesis and Photocatalytic Activity of Perovskite Niobium Oxynitrides with Wide Visible-light Absorption Bands. *ChemSusChem* **2011**, *4* (1), 74–78.

(52) Lei, S.; Cheng, D.; Gao, X.; Fei, L.; Lu, W.; Zhou, J.; Xiao, Y.; Cheng, B.; Wang, Y.; Huang, H. A New Low-Temperature Solution Route to Aurivillius-Type Layered Oxyluoride Perovskites  $Bi_2MOSF$  ( $M = Nb, Ta$ ) as Photocatalysts. *Applied Catalysis B: Environmental* **2017**, *205*, 112–120.

(53) Ishikawa, A.; Takata, T.; Kondo, J. N.; Hara, M.; Kobayashi, H.; Domen, K. Oxysulfide  $Sm_2Ti_2S_2O_5$  as a Stable Photocatalyst for Water Oxidation and Reduction under Visible Light Irradiation ( $\lambda \leq 650$  nm). *J. Am. Chem. Soc.* **2002**, *124* (45), 13547–13553.

(54) Ishikawa, A.; Takata, T.; Matsumura, T.; Kondo, J. N.; Hara, M.; Kobayashi, H.; Domen, K. Oxysulfides  $Ln_2Ti_2S_2O_5$  as Stable

Photocatalysts for Water Oxidation and Reduction under Visible-Light Irradiation. *J. Phys. Chem. B* **2004**, *108* (8), 2637–2642.

(55) Wang, R.; Liang, F.; Wang, F.; Guo, Y.; Zhang, X.; Xiao, Y.; Bu, K.; Lin, Z.; Yao, J.; Zhai, T.; et al.  $Sr_6Cd_2Sb_6O_7S_{10}$ : Strong SHG Response Activated by Highly Polarizable Sb/O/S Groups. *Angew. Chem., Int. Ed.* **2019**, *58* (24), 8078–8081.

(56) Allen, J. P.; Carey, J. J.; Walsh, A.; Scanlon, D. O.; Watson, G. W. Electronic Structures of Antimony Oxides. *J. Phys. Chem. C* **2013**, *117* (28), 14759–14769.

(57) Wang, X.; Li, Z.; Kavanagh, S. R.; Ganose, A. M.; Walsh, A. Lone Pair Driven Anisotropy in Antimony Chalcogenide Semiconductors. *arXiv (Condensed Matter: Materials Science)*, September 16, 2021, 2109.08117.

(58) Wang, V.; Xu, N.; Liu, J.-C.; Tang, G.; Geng, W.-T. VASPKIT: A User-Friendly Interface Facilitating High-Throughput Computing and Analysis Using VASP Code. *Comput. Phys. Commun.* **2021**, *267*, 108033.

(59) Gamon, J.; Giaume, D.; Wallez, G.; Labégorre, J.-B.; Lebedev, O.; Al Rahal Al Orabi, R.; Haller, S.; Le Mercier, T.; Guilmeau, E.; Maignan, A.; et al. Substituting Copper with Silver in the BIMOCh Layered Compounds ( $M = Cu$  or  $Ag$ ;  $Ch = S, Se$ , or  $Te$ ): Crystal, Electronic Structure, and Optoelectronic Properties. *Chem. Mater.* **2018**, *30* (2), 549–558.

(60) Hiramatsu, H.; Ueda, K.; Ohta, H.; Hirano, M.; Kikuchi, M.; Yanagi, H.; Kamiya, T.; Hosono, H. Heavy Hole Doping of Epitaxial Thin Films of a Wide Gap P-Type Semiconductor,  $LaCuOSe$ , and Analysis of the Effective Mass. *Appl. Phys. Lett.* **2007**, *91* (1), 012104.

(61) Wang, X.; Li, Z.; Kavanagh, S. R.; Ganose, A. M.; Walsh, A. Lone Pair Driven Anisotropy in Antimony Chalcogenide Semiconductors. *Phys. Chem. Chem. Phys.* **2022**, *24* (12), 7195–7202.

(62) Mohn, C. E.; Stölen, S. Influence of the Stereochemically Active Bismuth Lone Pair Structure on Ferroelectricity and Photocatalytic Activity of Aurivillius Phase  $Bi_2WO_6$ . *Phys. Rev. B* **2011**, *83* (1), 014103.

(63) Hu, C.; Zhang, B.; Lei, B.-H.; Pan, S.; Yang, Z. Advantageous Units in Antimony Sulfides: Exploration and Design of Infrared Nonlinear Optical Materials. *ACS Appl. Mater. Interfaces* **2018**, *10* (31), 26413–26421.

(64) Hu, C.; Mutailipu, M.; Wang, Y.; Guo, F.; Yang, Z.; Pan, S. The Activity of Lone Pair Contributing to SHG Response in Bismuth Borates: A Combination Investigation from Experiment and DFT Calculation. *Phys. Chem. Chem. Phys.* **2017**, *19* (37), 25270–25276.

(65) Walsh, A.; Payne, D. J.; Egdell, R. G.; Watson, G. W. Stereochemistry of Post-Transition Metal Oxides: Revision of the Classical Lone Pair Model. *Chem. Soc. Rev.* **2011**, *40* (9), 4455–4463.

(66) Payne, D. J.; Egdell, R. G.; Walsh, A.; Watson, G. W.; Guo, J.; Glans, P.-A.; Learmonth, T.; Smith, K. E. Electronic Origins of Structural Distortions in Post-Transition Metal Oxides: Experimental and Theoretical Evidence for a Revision of the Lone Pair Model. *Physical review letters* **2006**, *96* (15), 157403.

(67) Shaikh, S. K.; Inamdar, S. I.; Ganbavle, V. V.; Rajpure, K. Y. Chemical Bath Deposited ZnO Thin Film Based UV Photoconductive Detector. *J. Alloys Compd.* **2016**, *664*, 242–249.

(68) Inamdar, S.; Ganbavle, V.; Shaikh, S.; Rajpure, K. Effect of the Buffer Layer on the Metal-Semiconductor-Metal UV Photodetector Based on Al-doped and Undoped ZnO Thin Films with Different Device Structures. *physica status solidi (a)* **2015**, *212* (8), 1704–1712.

(69) Zhao, Q.; Wang, W.; Carrascoso-Plana, F.; Jie, W.; Wang, T.; Castellanos-Gomez, A.; Frisenda, R. The Role of Traps in the Photocurrent Generation Mechanism in Thin InSe Photodetectors. *Materials Horizons* **2020**, *7* (1), 252–262.

(70) Shi, Y.-F.; Li, X.-F.; Zhang, Y.-X.; Lin, H.; Ma, Z.; Wu, L.-M.; Wu, X.-T.; Zhu, Q.-L.  $[(Ba_19Cl_4)(Ga_6Si_{12}O_{42}S_8)]$ : A Two-Dimensional Wide-Band-Gap Layered Oxysulfide with Mixed-Anion Chemical Bonding and Photocurrent Response. *Inorganic chemistry* **2019**, *58* (10), 6588–6592.

(71) Ogisu, K.; Ishikawa, A.; Shimodaira, Y.; Takata, T.; Kobayashi, H.; Domen, K. Electronic Band Structures and Photochemical

Properties of La- Ga-Based Oxysulfides. *J. Phys. Chem. C* **2008**, *112* (31), 11978–11984.

(72) *Photoelectrochemical Water Splitting: Materials, Processes and Architectures*; Lewerenz, H.-J., Peter, L., Eds.; Royal Society of Chemistry: Cambridge, UK, 2013.

(73) Peter, L. M. Energetics and Kinetics of Light-Driven Oxygen Evolution at Semiconductor Electrodes: The Example of Hematite. *J. Solid State Electrochem.* **2013**, *17*, 315–326.

(74) Leroy, S.; Blach, J.-F.; Huvé, M.; Léger, B.; Kania, N.; Henninot, J.-F.; Ponchel, A.; Saitzek, S. Photocatalytic and Sonophotocatalytic Degradation of Rhodamine B by Nano-Sized La<sub>2</sub>Ti<sub>2</sub>O<sub>7</sub> Oxides Synthesized with Sol-Gel Method. *J. Photochem. Photobiol., A* **2020**, *401*, 112767.

(75) Bott, A. W. Electrochemistry of Semiconductors. *Curr. Sep.* **1998**, *17*, 87–92.

(76) Matsumoto, Y.; Omae, M.; Watanabe, I.; Sato, E. Photoelectrochemical Properties of the Zn-Ti-Fe Spinel Oxides. *J. Electrochem. Soc.* **1986**, *133* (4), 711.

(77) Kalanur, S. S. Structural, Optical, Band Edge and Enhanced Photoelectrochemical Water Splitting Properties of Tin-Doped WO<sub>3</sub>. *Catalysts* **2019**, *9* (5), 456.

(78) Lin, L.; Lin, J. M.; Wu, J. H.; Hao, S. C.; Lan, Z. Photovoltage Enhancement of Dye Sensitised Solar Cells by Using ZnO Modified TiO<sub>2</sub> Electrode. *null* **2010**, *14* (5), 370–374.

(79) Butler, M.; Ginley, D. Prediction of Flatband Potentials at Semiconductor-electrolyte Interfaces from Atomic Electronegativities. *J. Electrochem. Soc.* **1978**, *125* (2), 228.

(80) Xu, Y.; Schoonen, M. A. The Absolute Energy Positions of Conduction and Valence Bands of Selected Semiconducting Minerals. *Am. Mineral.* **2000**, *85* (3–4), 543–556.

(81) Castelli, I. E.; Landis, D. D.; Thygesen, K. S.; Dahl, S.; Chorkendorff, I.; Jaramillo, T. F.; Jacobsen, K. W. New Cubic Perovskites for One-and Two-Photon Water Splitting Using the Computational Materials Repository. *Energy Environ. Sci.* **2012**, *5* (10), 9034–9043.

(82) Ohtani, B. Photocatalysis by Inorganic Solid Materials: Revisiting Its Definition, Concepts, and Experimental Procedures. *Adv. Inorg. Chem.* **2011**, *63*, 395–430.

(83) Luo, Y.; Qiao, L.; Wang, H.; Lan, S.; Shen, Y.; Lin, Y.; Nan, C. Bismuth Oxysulfide and Its Polymer Nanocomposites for Efficient Purification. *Materials* **2018**, *11* (3), 447.

(84) Ha, V.-A.; Ricci, F.; Rignanese, G.-M.; Hautier, G. Structural Design Principles for Low Hole Effective Mass S-Orbital-Based p-Type Oxides. *Journal of Materials Chemistry C* **2017**, *5* (23), 5772–5779.

(85) Liu, M.-L.; Wu, L.-B.; Huang, F.-Q.; Chen, L.-D.; Chen, I. A Promising P-Type Transparent Conducting Material: Layered Oxysulfide [Cu<sub>2</sub>S<sub>2</sub>][Sr<sub>3</sub>Sc<sub>2</sub>O<sub>3</sub>]. *J. Appl. Phys.* **2007**, *102* (11), 116108.

(86) Dong, X.-D.; Zhang, Y.-M.; Zhao, Z.-Y. Role of the Polar Electric Field in Bismuth Oxyhalides for Photocatalytic Water Splitting. *Inorg. Chem.* **2021**, *60* (12), 8461–8474.

(87) Lou, Z.; Wang, P.; Huang, B.; Dai, Y.; Qin, X.; Zhang, X.; Wang, Z.; Liu, Y. Enhancing Charge Separation in Photocatalysts with Internal Polar Electric Fields. *ChemPhotoChem.* **2017**, *1* (5), 136–147.

(88) Dong, X.-D.; Yao, G.-Y.; Liu, Q.-L.; Zhao, Q.-M.; Zhao, Z.-Y. Spontaneous Polarization Effect and Photocatalytic Activity of Layered Compound of BiOIO<sub>3</sub>. *Inorg. Chem.* **2019**, *58* (22), 15344–15353.

(89) Chen, F.; Huang, H.; Guo, L.; Zhang, Y.; Ma, T. The Role of Polarization in Photocatalysis. *Angew. Chem., Int. Ed.* **2019**, *58* (30), 10061–10073.

(90) Guo, Y.; Shi, W.; Zhu, Y. Internal Electric Field Engineering for Steering Photogenerated Charge Separation and Enhancing Photoactivity. *EcoMat* **2019**, *1* (1), No. e12007.

(91) Chen, J.; Zhai, Y.; Yu, Y.; Luo, J.; Fan, X. Spatial Separation of Photo-Induced Charge Carriers in a Na<sub>3</sub>VO<sub>2</sub>B<sub>6</sub>O<sub>11</sub> Polar Material and Its Enhanced Photocatalytic Activity. *Appl. Surf. Sci.* **2021**, *556*, 149809.

## NOTE ADDED AFTER ASAP PUBLICATION

This paper was published on October 23, 2023, with missing Supporting Information files. The corrected version was posted on November 2, 2023.